Thermokarst amplifies fluvial inorganic carbon cycling and export across watershed scales on the Peel Plateau, Canada

Scott Zolkos[1,†], Suzanne E. Tank[1], Robert G. Striegl[2], Steven V. Kokelj[3], Justin Kokoszka[3], Cristian Estop-Aragonés[4,¥], David Olefeldt[4]

5 [1]Department of Biological Sciences, University of Alberta, Edmonton, AB, T6G 2E3 Canada
[2]USGS National Research Program, Boulder, CO, 80303 USA
[3]Northwest Territories Geological Survey, Yellowknife, NT, X1A 2L9 Canada
[4]Department of Renewable Resources, University of Alberta, Edmonton, AB, T6G 2E3 Canada
[†]Present address: Woods Hole Research Center, Falmouth, MA 02540 USA
10 [¥]Present address: Institute of Landscape Ecology, University of Münster, Münster, 48149 Germany

Correspondence to: Scott Zolkos (sgzolkos@gmail.com)

Abstract. The chemical weathering of minerals is a primary control on atmospheric CO_2 levels and Earth's climate over geological timescales. As climate warming and precipitation intensify at high latitudes, glaciated terrains across the circumpolar north are poised for rapid geomorphic change and associated changes in mineral weathering

15 dynamics. Here, we determine how the effects of permafrost thaw on mineral weathering sources and inorganic carbon cycling and export integrate across watershed scales (from ~2 to 1000 km²) in a permafrost terrain within a former glacial margin and dominated by relatively inorganic sediments (Peel Plateau, Canada). Our work was conducted along three nested transects with varying intensities of retrogressive thaw slump (RTS) thermokarst activity: a 550 m transect along a first-order thaw stream within a RTS; a 14 km transect along a stream which

20 directly received RTS inputs; and a 70 km transect along a larger stream which received inputs from RTS-affected tributaries. In the thaw stream, rapid sulfuric acid weathering of carbonate tills appeared to amplify CO_2 efflux to the atmosphere and HCO_3^- export downstream, where DIC and CO_2 stable isotopes revealed a shift to an abiotic-inorganic driven aquatic carbon cycle. Along the intermediate transect, DIC concentrations were ten times higher in the RTS-affected reach than in the undisturbed headwaters, and decreased downstream with decreasing RTS area.

25 Along the largest transect, HCO_3^- concentrations increased by two orders of magnitude in association with RTS activity, despite RTSs covering only ~0.5% of the landscape. Statistical modeling of hydrochemical measurements and geospatial landscape data showed that RTSs were a primary landscape driver of HCO_3^- export across watershed scales. Constraining sources and rates of mineral weathering across diverse permafrost terrains will help to understand future changes in Arctic aquatic carbon cycling, as our results suggest that abiotic-inorganic processes

30 may become prevalent.

1 Introduction

The chemical weathering of minerals is a fundamental control on atmospheric CO_2 levels over geological timescales and thus Earth's long-term climate (Berner, 1999). Rapid modern warming at northern latitudes (Serreze and Barry, 2011) is driving a suite of changes including the degradation of the cryosphere (Biskaborn et al., 2019), increasing

35 vegetation productivity (Bjorkman et al., 2018), intensifying hydrologic cycles (Rawlins et al., 2010), and

strengthening land-freshwater linkages (Vonk et al., 2019; Walvoord and Kurylyk, 2016). These processes are activating large amounts of mineral substrate into biogeochemical cycles, with significant implications for the rate and magnitude of mineral weathering over modern timescales (Lacelle et al., 2019; Wadham et al., 2019). In recent decades, fluxes of carbonate alkalinity (HCO_3^-, CO_3^{2-}) and solutes in rivers across the circumpolar north have

40   increased and more than doubled in some regions (Drake et al., 2018a; Tank et al., 2016; Toohey et al., 2016; Zolkos et al., 2018). This intensification of dissolved inorganic carbon (DIC = $\Sigma[CO_2, HCO_3^-, CO_3^{2-}]$) cycling reflects enhanced mineral weathering associated with a thickening of the active layer, deepening hydrologic flowpaths into mineral soils, and greater soil acidity associated with increasing vegetation productivity (Drake et al., 2018a; Tank et al., 2016; Toohey et al., 2016). Coupled to these processes, carbonate equilibrium reactions along the

45   land-freshwater continuum determine the balance of DIC species and therefore its susceptibility to atmospheric exchange as CO_2 versus export to the ocean as alkalinity (Stumm and Morgan, 1996).

From a geochemical perspective, three coupled factors primarily influence the magnitude and directionality of mineral weathering within climate feedbacks: the mineral composition of substrate; the acid responsible for chemical weathering; and the rate of weathering (Stumm and Morgan, 1996). First, half of riverine carbonate

50   alkalinity exported to the ocean is returned to the atmosphere over geological timescales by precipitation reactions within the marine carbon cycle (Calmels et al., 2007). Hence, silicate weathering by atmospheric or soil respiration CO_2 dissolved in water (carbonic acid, H_2CO_3) represents a long-term CO_2 sink, as this process generates alkalinity without liberating mineral carbon. In contrast, carbonate weathering by H_2CO_3 is a CO_2 sink only over shorter timescales, as half of the alkalinity produced is geogenic. HCO_3^- produced during carbonate weathering in the

55   presence of strong acids, for instance sulfuric acid (H_2SO_4) from sulfide oxidation, is thus a CO_2 source. Second, these reactions demonstrate how the mineral composition of a substrate and the acids responsible for its weathering can influence the degree to which weathering is a CO_2 source or sink. Lastly, rates of chemical weathering are orders of magnitude faster for carbonates and sulfides than for silicates (Stumm and Morgan, 1996). Further, weathering rates generally increase with mineral surface area, and therefore are generally fast in glacial

60   environments owing to intense physical weathering (Anderson, 2007). Indeed, hydrochemical signatures of trace carbonate and sulfide lithologies can dominate weathering fluxes in primarily silicate glacial environments (Anderson, 2007). The disparity is so significant that, when sediment supplies are sufficient, H_2CO_3 carbonate weathering in proglacial streams can consume dissolved CO_2 to below atmospheric levels (Sharp et al., 1995; St. Pierre et al., 2019).

65   Glaciated permafrost terrains are poised for rapid geomorphic and associated biogeochemical change as the climate warms and precipitation intensifies at high latitudes (Kokelj et al., 2017b). Areas currently with glacial coverage are of particular interest, owing to increased understanding of their effects on atmospheric CO_2 levels and long-term global climate (St. Pierre et al., 2019; Torres et al., 2017). Despite glacial retreat across much of the circumpolar north – most notably the Laurentide Ice Sheet (LIS) – lasting biogeochemical legacies remain preserved within these

70   vast landscapes (Kokelj et al., 2017b). In North America, the comminution of carbonate and shale bedrock during the LIS expansion and the climate and vegetative protection of ice- and sediment-rich tills in the wake of its retreat

endowed former glacial margins across northwestern Canada with relatively inorganic, ice-rich permafrost (Kokelj et al., 2017b). Today, the climate-driven renewal of post-glacial landscape change is mobilizing immense stores of minerals into modern biogeochemical cycles (Kokelj et al., 2017a). On the Peel Plateau (NWT, Canada),

75 retrogressive thaw slumps (RTSs) expose carbonate- and sulfide-bearing glaciogenic permafrost sediments that are tens of meters in thickness. The chemical weathering and fluvial transport of these sediments results in increased HCO_3^- immediately downstream and greater solute and sediment loads throughout downstream systems (Kokelj et al., 2013; Malone et al., 2013; Zolkos et al., 2018). Yet, it remains unknown how thermokarst effects on mineral weathering and DIC sources and cycling integrate across watershed scales on the Peel Plateau and in relatively

80 inorganic-rich permafrost terrains elsewhere. These terrains, which are thought to occur within former glacial limits across the northern permafrost zone (Zolkos et al., 2018), represent a frontier with respect to current knowledge on carbon cycling and climate feedbacks.

In this study we evaluated trends in major ions, DIC concentration, and dual DIC and CO_2 stable isotopes along transects within three nested watersheds in the Stony Creek watershed (1100 km²) on the Peel Plateau. The three

85 transects spanned gradients of thermokarst disturbance: (i) a 550 m thaw stream formed by a runoff channel within an active retrogressive thaw slump (RTS FM2 runoff); (ii) a 14 km transect in a creek which originated in undisturbed headwaters, but was directly affected by RTS FM2 and additional RTSs along the studied reach (Dempster Creek); and (iii) a 70 km transect in a large stream which received inputs from multiple large RTS-affected tributaries and was itself a major tributary of the 70,000 km² Peel River watershed (Stony Creek) (Fig. 1).

90 Our nested watershed approach and comparisons of stream chemistry between undisturbed headwaters and thermokarst-affected reaches enabled us to develop a novel conceptual model which details how RTS effects on inorganic carbon cycling integrate across watershed scales. These results help to bring abiotic-inorganic aquatic processes into our conceptualization of thermokarst effects on carbon cycling, which to-date have been driven by studies outside of former glacial limits and focused on organically-driven processes (Vonk et al., 2015).

95 **2 Methods**

2.1 Study Area

The Stony Creek watershed is located southwest of the hamlet of Fort McPherson, in the northern, or lower Peel River watershed (Fig. 1). Stony Creek, a tributary of the Peel River, originates in the Richardson Mountains, where the slopes are sparsely vegetated and mainly consist of colluvium from exposed marine shale and sandstone bedrock

100 (Norris, 1985). As Stony Creek flows eastward, the main channel and its tributaries incise ice-rich glacial deposits and underlying Cretaceous bedrock, forming a stream network comprised of tundra flow tracks grading to incised gravel bed streams with increasing watershed size. The fluvially-incised valleys and increasing regional precipitation have proven conducive to thaw-driven mass wasting of ice-rich glacial deposits and formation of RTSs (Kokelj et al., 2017b). RTS growth is driven by the ablation of exposed ground ice and is perpetuated by the

105 downslope mass wasting of thawed material via fluidized earth flows, which can accumulate large volumes of debris in stream valleys (Fig. 1). Across the Stony Creek watershed, intensifying RTS activity releases large volumes of

sediment and solutes into streams relative to undisturbed headwaters (Kokelj et al., 2017b; Segal et al., 2016). This substrate is transported to streams via rill runoff channels in the scar zone and debris tongue deposits in the stream valley. Impacts to Stony Creek are representative of numerous other major Peel River tributaries that have incised

110 the ice-rich Peel Plateau (Kokelj et al., 2015). The ~60 km^2 watershed of Dempster Creek, a tributary of Stony Creek, originates in willow and open spruce taiga without RTS activity, receiving large inputs of sediments and solutes from RTSs FM2 and FM3 within several kilometers of the headwaters (Kokelj et al., 2013; Malone et al., 2013). Many small, non-RTS affected streams and several larger RTS-affected tributaries flow into Dempster Creek before its confluence with Stony Creek.

115 **2.2 Stream Sampling**

In late July, 2017, we sampled three nested transects: (i) at five locations along a 550 m-long transect within the RTS FM2 rill runoff channel (Fig. 1a); (ii) Dempster Creek in the undisturbed headwaters, along its RTS-affected reach upstream of three major tributaries, and from the tributaries near their mouths, to characterize the downstream effects of RTS FM2 on DIC; (iii) Stony Creek in the undisturbed headwaters, along the RTS-affected reach of Stony

120 Creek upstream of seven major tributaries, and from the tributaries near their mouths, to determine RTS effects on DIC across broader scales (Fig. 1, Table A1). While the Dempster and Stony Creek headwater sites were not affected by RTSs, mainstem and tributary sampling sites were (Table A1). Minor tributaries of Dempster and Stony Creek, many of which were not affected by RTSs, were not sampled.

At all sampling sites, stream temperature and pH were measured using a pre-calibrated YSI Professional-Plus water

125 quality meter. At most sites, water samples were collected for ions, DIC, CO_2, CH_4, dissolved organic carbon (DOC), UV-visible absorbance, and total suspended sediments (TSS). Along the RTS FM2 runoff transect, we sampled only for DIC and CO_2 concentration, and stable isotopes of dissolved CO_2 ($\delta^{13}C_{CO2}$). One day prior, additional parameters were sampled at runoff site five, located near the confluence of the RTS runoff with Dempster Creek, for comparison with the full suite of chemistry parameters collected along the Dempster Creek transect. At

130 the Dempster and Stony Creek sites, we additionally sampled water for stable isotopes of DIC ($\delta^{13}C_{DIC}$) and $\delta^{13}C_{CO2}$ and used dual DIC and CO_2 stable isotopes to characterize abiotic and biotic processes influencing DIC sources and cycling.

Water samples were collected from the thalweg where possible, as an integrated sample from ~15 cm below the surface to ~1 m depth. An additional sample for TSS was collected in a 1 L HDPE in the same fashion. Water

135 samples were filtered using sample-rinsed 0.45 μm polyethersulfone (PES, ThermoFisher) or cellulose-acetate (CA, Sartorius) membranes. Samples for DIC were collected without headspace in airtight syringes. Samples for ions, DOC, and UV-visible absorbance were collected in acid washed (24 h, 10% v/v HCl) all-plastic syringes. Syringes were triple sample-rinsed, sealed without headspace, and stored cool and dark until processing within 10 h. Water for DIC was filtered (PES) into precombusted (5 h, 500˚C) glass vials without headspace and sealed with a butyl

140 rubber septum for DIC concentration or two silicone-teflon septa for $\delta^{13}C_{DIC}$. Samples for cations were filtered (CA)

into acid-washed bottles and acidified with trace metal-grade HNO_3, while anions were filtered (CA) but not acidified. Samples for DOC were filtered (PES) into precombusted glass vials and acidified to pH < 2 using trace metal-grade HCl (Vonk et al., 2015). Samples for UV-visible absorbance were filtered (PES) into non-acid washed 30 mL HDPE bottles. Samples were refrigerated (4°C, dark) until analysis.

145 Dissolved gases were collected following the headspace equilibration method (Hesslein et al., 1991) and stored in airtight syringes (for CO_2 concentration) or over-pressurized in pre-evacuated serum bottles sealed with pre-baked (60°C, 12 h), gas-inert butyl rubber stoppers (for $\delta^{13}C_{CO2}$, CH_4). At each site, atmospheric samples for CO_2 and CH_4 concentration and $\delta^{13}C_{CO2}$ were stored in the same fashion. Gas samples were stored in the dark at ~20°C prior to analysis within 10 h (CO_2) or two months ($\delta^{13}C_{CO2}$). Water and air temperature, atmospheric pressure, and the
150 volumetric ratio of sample to atmospheric headspace was recorded for correcting later calculations of CO_2 partial pressure (pCO_2) and $\delta^{13}C_{CO2}$ (Hamilton and Ostrom, 2007).

2.3 Stream Flow

Discharge (Q) in Stony Creek tributaries was estimated from a hydraulic geometry model (Gordon, 2004) that we developed using flow measurements made in Peel Plateau streams during 2015-2017 and width (W) estimated from
155 on-site measurements or photos from 2017 with a known scale. The model reflected measurements spanning diverse stream morphologies (W = 0.4–6.6 m) and flow conditions (Q = 0.005–0.91 m^3 s^{-1}):

$$Q = 10^{\log(W / 6.258) / 0.661} \quad (p < 0.01, R^2 = 0.89, n = 20) \quad (1)$$

Discharge values from 2015-2017 were calculated from measurements of stream flow (RedBack Model RB1, PVD100) and cross-sectional area made at increments equal to 10% of stream width (Gordon, 2004; Lurry and
160 Kolbe, 2000), and were averaged for sites with multiple measurements.

2.4 Geochemical Analyses

Upon returning from the field each day, CO_2 was measured using an infrared gas analyzer (PP Systems EGM-4). The EGM-4 was checked monthly for drift using a commercial standard (Scotty Gases). We calculated pCO_2 using Henry's constants corrected for stream water temperature (Weiss, 1974) and accounting for the ratio of water
165 volume to headspace during sample equilibration. DIC samples were measured by infrared CO_2 detection (LiCOR 7000) following acidification within a DIC analyzer (Apollo SciTech model AS-C3). Calibration curves were made daily using certified reference material (CRM) from Scripps Institution of Oceanography. Samples with DIC concentrations < 400 µM were analyzed using solutions prepared from a 1000 ppm TIC stock (ACCUSPEC) that were calibrated with CRM. DIC species (CO_2, HCO_3^-, CO_3^{2-}) were calculated from DIC concentration and pCO_2 or
170 pH using CO2sys (v.2.3) (Pierrot et al., 2006), using field temperature and pressure at the time of sampling, and the freshwater equilibrium constants for K1 and K2 (Millero, 1979).

Cations and trace elements were measured by optical emission spectrometry (Thermo ICAP-6300) and anions by ion chromatography (Dionex DX-600) at the University of Alberta Biogeochemical Analytical Services Laboratory (BASL, ISO/EIC accreditation #17025). DOC was measured using a total organic carbon analyzer (Shimadzu
175   5000A). DOC standard curves were made daily with a 1000 ppm KHP solution (ACCUSPEC) and an in-house caffeine standard (10 mg L^{-1}) was run every 20 samples to monitor instrument drift. Absorbance spectra were analyzed using an Ocean Optics UV-VIS instrument with a Flame spectrometer module, following Stubbins et al. (2017) and corrected for Fe interference (Poulin et al., 2014). To evaluate organic carbon reactivity, we used specific ultraviolet absorbance at 254 nm (SUVA$_{254}$) to infer DOC aromaticity (Weishaar et al., 2003).

180   $\delta^{13}C_{DIC}$ was determined using an isotope ratio mass spectrometer (Finnigan Mat DeltaPlusXP) interfaced to a total organic carbon analyzer (OI Analytical Aurora Model 1030W) at the University of Ottawa Stable Isotope Laboratory. $\delta^{13}C_{CO2}$ and CH$_4$ concentration were analyzed within two months using a Picarro isotope analyzer (G2201-*i*; < 0.2‰ precision, CH$_4$ operational range = 1.8–1500 ppm) equipped with an injection module for discrete samples (SSIM). Commercial $\delta^{13}C_{CO2}$ and CH$_4$ standards were used to check for drift during each run. We used
185   mass balance to correct $\delta^{13}C_{CO2}$ values for the $\delta^{13}C$ and mass of atmospheric CO$_2$ used for equilibration (Hamilton and Ostrom, 2007). To assess $\delta^{13}C_{CO2}$ fractionation from calcite precipitation (Turner, 1982) and methanogenesis (Campeau et al., 2018) in RTS FM2 runoff, we calculated the saturation index (SI) and partial pressure of CH$_4$ (*p*CH$_4$). SI was calculated using the hydrochemical software Aqion version 6.7.0 (http://www.aqion.de), which uses the U.S. Geological Survey software PHREEQC (Parkhurst and Appelo, 2013) as the internal numerical solver.
190   Samples for atmospheric and dissolved CH$_4$ were collected in the same fashion as $\delta^{13}C_{CO2}$. *p*CH$_4$ was calculated using Bunsen solubility coefficients (Wiesenburg and Guinasso, 1979) converted to the appropriate units (Sander, 2015).

TSS samples were filtered onto muffled (450˚C, 4 h) and pre-weighed glass fiber filters (Whatman GF/F; 0.7 µm nominal pore size) upon returning from the field, stored frozen, and dried (60˚C, 24 h) for gravimetric analysis
195   following a modified version of U.S. Geological Survey Method I-3765.

2.5 Mineral Weathering and DIC Sources

We used a Piper diagram, which reflects the proportional equivalent concentrations of ions in a sample relative to mineral weathering end-members, to constrain the sources of mineral weathering and HCO$_3^-$. The products of Eq. A1–A7 defined the mineral weathering end-members in the Piper diagram (Table A2). We further constrained
200   mineral weathering and DIC sources using $\delta^{13}C_{DIC}$ and pH. End-member $\delta^{13}C_{DIC}$ ranges for equilibrium processes (mixing with atmospheric and/or biotic CO$_2$) and kinetic reactions (mineral weathering) were derived following Lehn et al. (2017).

To evaluate potential effects on $\delta^{13}C_{CO2}$ from DIC speciation along the pH continuum (Eq. A8) (Clark and Fritz, 1997), we compared theoretical and observed $\delta^{13}C_{CO2}$ values in the Stony Creek mainstem. Theoretical $\delta^{13}C_{CO2}$

205   values were calculated using mass balance to obtain $\delta^{13}C_{HCO3}$ from measurements of DIC, CO_2, HCO_3^-, $\delta^{13}C_{DIC}$, and

$\delta^{13}C_{CO2}$. We then used measurements of stream temperature (T) to calculate the equilibrium fractionation between

CO_2 and HCO_3^- ($\varepsilon = -9.483 \times 10^3/T + 23.89‰$; Mook et al., 1974). Finally, ε was subtracted from $\delta^{13}C_{HCO3}$ to

obtain theoretical $\delta^{13}C_{CO2}$. Similarity between observed and theoretical $\delta^{13}C_{CO2}$ values was interpreted as $\delta^{13}C_{CO2}$

variability driven by carbonate equilibrium reactions, whereas dissimilarity was taken to reflect effects from CO_2

210   degassing (Zhang et al., 1995) and/or biotic CO_2 production (Kendall et al., 2014).

2.6 Geospatial Analyses

Stream networks and watershed areas were delineated in ArcGIS 10.5 from the gridded (30 m) Canadian Digital

Elevation Model (CDEM). To statistically assess landscape controls on DIC cycling (Sect. 2.7), we delineated active

RTSs and derived terrain roughness and vegetation productivity in the major tributary watersheds of Stony Creek.

215   RTSs were interpreted as active where exposed sediment visibly dominated the feature surface (Cray and Pollard,

2015) in orthorectified SPOT multispectral imagery that we pan-sharpened to 1.6 m resolution using the ArcGIS

Image Analysis tool. The satellite imagery was collected from September 9 to 25, 2016. Active RTSs that were

connected to streams were manually delineated using ArcGIS. We used RivEx 10.25 software (Hornby, 2017) to

quantify the number of active RTSs impacting streams in the Stony Creek watershed and to visualize RTS impact

220   accumulation across the fluvial network. We defined RTS impact accumulation as the cumulative number of active

RTSs impacting upstream reaches. RTSs were interpreted to impact streams based on contact or interpreted

downslope flow based on slope direction and gradient from the CDEM (Supplementary Information). Where a

single RTS affected multiple streams, only the upstream segment was used for the accumulation.

We used the Geomorphic and Gradients Metrics Toolbox (Evans et al., 2014) to calculate terrain roughness, which

225   is a measure of variance across a land surface and represents topographic complexity (Riley et al., 1999). We use

terrain roughness as a proxy for potential physical erosion, which is known to enhance sulfide oxidation by exposing

shale regolith throughout the Peel River watershed (Calmels et al., 2007) and may therefore influence DIC. The

enhanced vegetation index (EVI) was used to broadly evaluate vegetation productivity (Huete et al., 2002), which is

known to influence DIC production by enhancing mineral weathering (Berner, 1999). We used the U.S. National

230   Aeronautics and Space Administration EVI product (Didan, 2015), which is derived from gridded (250 m) moderate

resolution imaging spectroradiometer (MODIS). The MODIS data were collected on July 28, 2017. The ArcGIS

Zonal Statistics tool was used to calculate total RTS area, mean terrain roughness, and mean EVI in Stony Creek

tributary watersheds.

2.7 Statistics

235   We tested for downstream change in HCO_3^- concentration and pCO_2 along the Stony Creek mainstem using the non-

parametric Mann-Kendall test from the R software (R Core Team, 2018) package *zyp* (Bronaugh and Werner, 2013),

following the trend pre-whitening approach detailed by Yue et al. (2002) to account for serial autocorrelation. We

developed a multiple linear regression model to evaluate the influence of RTS activity on HCO_3^- export in Stony

240   Creek tributary watersheds relative to hydrology, terrain roughness, and vegetation productivity. To account for potential effects of varying tributary watershed areas on discharge (Q) and constituent concentration, we used tributary HCO_3^- yields in the model. Instantaneous discharge (Q, $m^3 s^{-1}$) was estimated from the hydraulic geometry relationship between Q and stream width (Eq. 1). Discharge and HCO_3^- flux (concentration*Q) were normalized to the respective tributary watershed area and scaled to estimate daily water yield (cm d^{-1}) and HCO_3^- yield (μmol m^{-2} d^{-1}). Daily HCO_3^- yields in Stony Creek tributaries were modeled as:

245
$$HCO_3^- \text{ yield} = RTS_n + RTS_{area} + \text{Water yield} + TR + EVI \quad (2)$$

where RTS_n is the number of active RTSs; RTS_{area} is the watershed area disturbed by RTSs (%); TR is the mean terrain roughness (m); and EVI is the mean enhanced vegetation index (–1 to 1). The multiple linear regression was trimmed using the *step* function in the R package *lmerTest* (Kuznetsova et al., 2018) to eliminate covariates which did not improve the model. Highly collinear covariates were identified using a Variance Inflation Factor > 3 (Zuur et

250   al., 2010) and removed from the trimmed models. Model fits were inspected visually with residual plots and covariates were transformed as needed to meet assumptions of independent and homoscedastic residuals (Zuur, 2009). Statistics were performed in the R programming environment (v.3.4; R Core Team, 2018) and significance was interpreted at $\alpha = 0.05$. To understand potential effects from variable rainfall on water yields prior to and during the two-day sampling window of the Stony Creek tributaries, we inspected total rainfall in 24 h increments

255   preceding the sampling of each Stony Creek tributary. Hourly rainfall data were obtained from a Government of Northwest Territories Total meteorological station located ~1 km from the RTS FM2 (Fig. 1).

3 Results and Discussion

3.1 Rapid Inorganic Carbon Cycling within a Permafrost Thaw Stream

Hydrochemical trends in the FM2 runoff transect were distinct compared to the Dempster and Stony Creek and

260   showed that RTS activity enhanced chemical weathering, CO_2 production, and fluvial export of HCO_3^-. Concentrations of HCO_3^- were up to two orders of magnitude greater in the runoff of RTS FM2 (1510 μM) than in the Dempster and Stony Creek headwaters (1–115 μM), where RTSs were absent (Table 1, Fig. 2). Building on previous findings (Kokelj et al., 2013; Malone et al., 2013; Zolkos et al., 2018), the increase in conductivity along the RTS FM2 runoff transect (from 1370 to 1986 μS cm^{-1}) demonstrates that, upon thaw, minerals within regional

265   permafrost tills readily weather during fluvial transport. Mineral weathering along the RTS FM2 runoff transect occurred in concert with a decrease in HCO_3^- from 1510 to 1386 μM (Table 1). The high proportion of SO_4^{2-} relative to other ions (Fig. 3) and ^{13}C-enriched $\delta^{13}C_{DIC}$ (–1.0‰) (Fig. 4) indicates that DIC was sourced from carbonate weathering by H_2SO_4 from sulfide oxidation (Clark and Fritz, 1997) and also suggests that sulfate salt (e.g. gypsum) dissolution added some SO_4^{2-}. Together, these trends reflect a strong coupling between mineral

270   weathering and DIC production following thaw and exposure of tills by thermokarst (Zolkos et al., 2018). Further, while HCO_3^- concentrations within the RTS FM2 runoff were high relative to undisturbed headwaters, the decrease

in HCO_3^- along the transect indicates that carbonate equilibrium reactions within RTSs on the Peel Plateau can rapidly transform HCO_3^- to CO_2 during fluvial transport.

The trends in HCO_3^-, pCO_2, and stable CO_2 isotopes along the RTS FM2 runoff transect indicated that H_2SO_4 from
275   sulfide oxidation contributed to CO_2 production in the upper reach near the RTS and that degassing along the lower reach resulted in CO_2 efflux to the atmosphere. Within the first 220 m, pCO_2 increased from 1046 to 1534 µatm and relatively ^{13}C-enriched $δ^{13}C_{CO2}$ (range = –11.4 to –12.1‰) (Table 1, Fig. 5) aligned with values expected from H_2SO_4 weathering of regional carbonate (–0.7 to –5.6‰) (Hitchon and Krouse, 1972), when accounting for isotopic fractionation of ~8‰ between carbonate and CO_2 at the temperature of FM2 runoff (18˚C) (Clark and Fritz, 1997).
280   These trends are consistent with some abiotic CO_2 production via carbonate weathering and HCO_3^- conversion to CO_2. After 220 m, pCO_2 decreased from 1534 to 742 µatm and $δ^{13}C_{CO2}$ values increased from –11.4 to –10‰, reflecting the preferential loss of ^{12}C in the CO_2 phase via DIC fractionation and degassing (Doctor et al., 2008; Drake et al., 2018b; Kendall et al., 2014). ^{13}C enrichment of the CO_2 pool by methanogenesis (Campeau et al., 2018), photosynthesis (Descolas-Gros and Fontungne, 1990), and/or calcite precipitation (Turner, 1982) was
285   unlikely, as CH_4 in FM2 runoff was relatively low (pCH_4 = 3.6 ± 1.9 µatm, mean ± SD, n = 6), the high turbidity of FM2 runoff likely inhibited photosynthesis, and calcite was below saturation (SI = –0.79). These observations of rapid CO_2 production along the upper reach of the transect and efflux along the lower reach align with recent estimates of high rates of CO_2 efflux within RTS runoff (Zolkos et al., 2019).

Our observations of downstream DIC transformation coupled to mineral weathering indicate that recently thawed
290   permafrost substrate can rapidly generate substantial HCO_3^- and some abiotic CO_2 during fluvial transport within RTS rill runoff. A majority of the DIC was exported to larger streams as HCO_3^-, while a smaller proportion was converted to CO_2 and degassed during fluvial transport within the RTS runoff. Similar to research on organic matter decomposition in Yedoma regions (Drake et al., 2018b), these results from a relatively inorganic-rich terrain demonstrate that thermokarst can promote rapid inorganic carbon cycling upon thaw and during fluvial transport in
295   meltwater thaw streams.

3.2 Abiotic-Inorganic Carbon Cycling in a Thermokarst-Affected Intermediate Watershed

Along the Dempster Creek transect, trends in HCO_3^- concentration, pCO_2, and stable isotopes reflected a clear shift in carbon cycling driven by biotic-organic processes in the undisturbed headwaters to abiotic-inorganic processes in the RTS-affected reach (Fig. 1). In the undisturbed Dempster Creek headwaters (site one), relatively low pH (5.82)
300   (Table 1), high pCO_2 (2467 µatm) (Fig. 2b), and low $δ^{13}C_{DIC}$ and $δ^{13}C_{CO2}$ values (Figs. 4, 5) reflected DIC that was primarily sourced from inputs of soil CO_2 and mixing with atmospheric CO_2 (Campeau et al., 2018; Kendall et al., 2014). The concentration of HCO_3^- was ten times lower in the undisturbed headwaters (115 µM) than at the downstream site nearest the FM2 runoff (site two, 1321 µM) (Table 1, Fig. 2a), where $δ^{13}C_{DIC}$ reflected H_2SO_4 carbonate weathering and inputs from the RTS runoff described above (Fig. 4). In conjunction with the increase in
305   HCO_3^- between Dempster Creek headwaters and the first RTS-affected sampling site, pCO_2 decreased (from 2467 to

686 μatm) and $\delta^{13}C_{CO_2}$ increased (from −21.6 to −16.0‰) (Table 1). Although DOC from RTS runoff is known to be relatively biolabile within streams on the Peel Plateau (Littlefair et al., 2017), these trends between the undisturbed headwaters and the first RTS-affected sampling site suggest stronger effects on DIC from CO_2 degassing to the atmosphere than from biotic CO_2 production associated with inputs of permafrost organic carbon from RTS activity

310   (Doctor et al., 2008; Drake et al., 2018b; Kendall et al., 2014). This may be partly due to the protection of DOC from microbial oxidation via adsorption to RTS sediments (Gentsch et al., 2015), which aligns with our observations of high TSS (11800 mg L^{-1}) and a decrease in DOC concentration downstream of RTS FM2 (Table 1, Fig. 6) (Littlefair et al., 2017). These trends are consistent with observations that substantial CO_2 is lost in headwaters via efflux to the atmosphere (Drake et al., 2018b) and also show that abiotic-inorganic processes can dominate carbon

315   cycling where thermokarst releases inorganic substrate into fluvial networks.

The hydrochemical trends along the RTS-affected reach of the Dempster Creek transect (sites 2–4) showed that the balance between inputs from RTS-affected and undisturbed streams moderated the magnitude of HCO_3^- export within downstream environments. The decrease in HCO_3^- (1321 to 946 μM; Fig. 2) and conductivity (958 to 416 μS cm^{-1}; Table 1) along the entire RTS-affected reach of the transect occurred in conjunction with inputs from dozens

320   of small, non RTS-affected tributary streams, suggesting that these streams were partly responsible for diluting the inputs from RTS activity. Further, the area of RTS disturbance within successive downstream watersheds decreased from 3.2 to 1.2% (Table 1), indicating that RTS inputs diminished relative to inputs from undisturbed areas of the Dempster Creek watershed. Despite some dilution, the high concentration of HCO_3^- and $\delta^{13}C_{DIC}$ enrichment near the mouth of Dempster Creek (Figs. 1, 4) indicate that H_2SO_4 carbonate weathering associated with RTS activity

325   enhanced HCO_3^- export far downstream.

In addition to HCO_3^-, RTSs on the Peel Plateau deliver a large amount of carbonate-bearing sediment to stream networks (Kokelj et al., 2015; Zolkos et al., 2018). We hypothesized that H_2CO_3 weathering of these sediments during fluvial transport may stimulate some CO_2 consumption (St. Pierre et al., 2019; Striegl et al., 2007). Along the RTS-affected reach of the Dempster Creek transect (sites 2–4, Fig. 1), pCO_2 decreased from 686 to 600 μatm (Fig.

330   2b). Yet, the coincident decreases in conductivity, HCO_3^-, and pH (Table 1, Figs. 2a, 4) suggest that dilution and degassing had stronger effects on the decreasing pCO_2 than did H_2CO_3 carbonate weathering. Although we observed a net decrease in pCO_2, the relatively depleted and decreasing $\delta^{13}C_{CO_2}$ values (Table 1, Fig. 5) indicate some contribution from biotic processes to pCO_2 supersaturation in the RTS-affected reach. This aligns with increasing concentrations of DOC which resembled the terrestrial-origin DOC in tributary streams (as inferred from $SUVA_{254}$)

335   (Table 1, Fig. 6), suggesting that tributary streams stimulated some microbial production of terrestrial-origin CO_2, and/or delivered ^{13}C-depleted (biotic) CO_2 to Dempster Creek.

Together, our observations along the RTS FM2 runoff (Sect. 3.1) and Dempster Creek (Sect. 3.2) transects suggest that rates of carbonate weathering and CO_2 degassing are most pronounced following thaw and within headwaters. These effects are less pronounced in mid-order streams like Dempster Creek, which mix with inputs from

 undisturbed tributaries, may receive and/or generate some biotic CO_2, and export HCO_3^- downstream at a magnitude coupled to the area of RTS disturbance.

3.3 Thermokarst Effects on HCO_3^- Export and CO_2 Production across a Major Watershed

Hydrochemical trends along the larger Stony Creek transect resembled those in Dempster Creek and showed that RTS activity strengthens signals of H_2SO_4 carbonate weathering and amplifies HCO_3^- export across watershed

345 scales. In the mountainous, non-RTS affected headwaters of Stony Creek, where bedrock lithologies contain limited carbonate, the Ca^{2+}–Mg^{2+}–SO_4^{2-}-type waters at site one (Fig. 3a) reflected the denudation of sulfide- and gypsum-bearing bedrock exposed in the Richardson Mountains (Norris, 1985). In these headwaters, pCO_2 near atmospheric equilibrium (Fig. 2), low HCO_3^- (33 μM) and pH (5.66), and intermediate $\delta^{13}C_{DIC}$ (–11.6‰) values indicated that mixing with atmospheric and biotic CO_2 were the primary sources of DIC (Fig. 4). Along the entire Stony Creek

350 transect, the striking increase in HCO_3^- (from 33 to 461 μM) (Tables 1, A1, Fig. 2a) together with ionic and $\delta^{13}C_{DIC}$ signals of intensified carbonate weathering (Figs. 3a, 4) reflect amplified inorganic carbon cycling associated with inputs from RTS-affected tributaries. Along Stony Creek, the RTS disturbance area increased from 0% in the undisturbed headwaters to $0.36 \pm 0.03\%$ (mean ± SD, $n = 5$) of the watersheds of sites four through eight (Table 1). This builds on the findings that solutes and sediments from RTSs cascade through fluvial networks (Kokelj et al.,

355 2013; Malone et al., 2013) and shows that RTS activity, despite covering less than 0.5% of the greater Stony Creek watershed, greatly increases fluvial HCO_3^- export to the Peel River.

While the concentration of HCO_3^- increased downstream along the entire Stony Creek transect, pCO_2 was slightly above atmospheric and relatively constant (479 ± 35 μatm, mean ± SD), suggesting a greater balance between CO_2 production and degassing to the atmosphere than in the RTS FM2 runoff or undisturbed headwaters. Yet, $\delta^{13}C_{CO2}$

360 values decreased downstream from –13.8 to –18.1‰ along Stony Creek (Fig. 5), indicating a shift in the processes influencing CO_2. To evaluate the relative influence of biotic CO_2 production, CO_2 conversion to HCO_3^-, and CO_2 degassing to the atmosphere on $\delta^{13}C_{CO2}$ values, we compared our measurements of $\delta^{13}C_{CO2}$ with theoretical values reflecting DIC controlled by speciation along the pH continuum (Eq. A8) (Sect. 2.5). From ~5 to 35 km downstream, the good agreement between measured and theoretical $\delta^{13}C_{CO2}$ values reflected equilibrium

365 fractionation ($\varepsilon = 9.7‰$ at 9°C; Mook et al., 1974) between CO_2 and HCO_3^- (Fig. 7). This suggests that carbonate equilibrium reactions coupled with increasing HCO_3^- from RTS-affected tributaries was a primary control on CO_2 along the upper reach of the Stony Creek transect. Along the lower reach of the transect, as DOC availability increased (Fig. 6), $\delta^{13}C_{CO2}$ values were lower than would be expected from degassing and/or CO_2 conversion to HCO_3^- (Fig. 7). This suggests that biotic CO_2 sustained the elevated pCO_2 downstream (Fig. 3b). Yet, this signal of

370 biotic CO_2 production was not evident in the ^{13}C-enriched $\delta^{13}C_{DIC}$ along Stony Creek (Table 1, Fig. 5), which reflected a geogenic DIC pool dominated by inputs of HCO_3^- from RTS-affected tributaries. These trends show that, in environments with abundant carbonate weathering, measuring both $\delta^{13}C_{CO2}$ and $\delta^{13}C_{DIC}$ can provide a more complete understanding of DIC sources and cycling (Horgby et al., 2019). From a carbon cycling perspective, these

375   trends in Stony Creek show that HCO$_3^-$ export across watershed scales is among the most striking legacies of regional thermokarst activity.

3.4 Landscape Controls on Inorganic Carbon Cycling in a Thermokarst-Affected Fluvial Network

In RTS-affected tributaries of Stony Creek (Fig. 1), HCO$_3^-$ yields (1070 ± 985 μmol m^{-2} d^{-1}, mean ± SD, n = 6) were several orders of magnitude higher than in the non-RTS affected headwaters (1.6 μmol m^{-2} d^{-1}) (Table 2) and approached summertime HCO$_3^-$ yields in watersheds with carbonate rock weathering by glacial activity (2700 to
380   3300 μmol m^{-2} d^{-1}) (Lafrenière and Sharp, 2005; Striegl et al., 2007). To determine the importance of RTS activity on HCO$_3^-$ export in Stony Creek tributary watersheds, we paired estimates of HCO$_3^-$ and water yields with geospatial data for active RTSs, terrain roughness, and vegetation productivity in a multiple linear regression model (Sect. 2.7). Water yield, the area of RTS disturbance, and terrain roughness were retained during automated covariate selection for the final model (F_3 = 45, p < 0.01, R^2 = 0.96). In addition to water yield, HCO$_3^-$ yield was
385   positively correlated with RTS disturbance area (Table 2). Terrain roughness was anticorrelated with HCO$_3^-$ yield, likely owing to relatively more limited carbonate weathering in the mountainous headwaters of the Stony Creek watershed, where exposed shale bedrock predominates (Norris, 1985) (Table 1). Low HCO$_3^-$: water yield in the Stony Creek headwaters (Table 2) further suggested that HCO$_3^-$ export was limited by carbonate availability rather than by water. Higher HCO$_3^-$: water yields in RTS-affected tributaries aligned with the model results indicating that
390   RTS activity increases inorganic carbon availability and export across watershed scales on the Peel Plateau.

These findings align with the observation that climate warming and intensifying precipitation has rejuvenated deglaciation-phase geomorphic and associated mineral weathering dynamics across the western Canadian Arctic (Kokelj et al., 2017a). Mineral weathering will likely come to dominate biogeochemical cycles in these regions, which may bear increasing hydrochemical resemblance to landscapes with glacial coverage (Anderson, 2007; St.
395   Pierre et al., 2019; Striegl et al., 2007; Wadham et al., 2019). Further, the considerable HCO$_3^-$ export within the Stony Creek watershed, where RTS spanned < 0.5% of the watershed, demonstrates that thermokarst development across a fractional proportion of ice- and sediment- rich landscapes can substantially intensify inorganic carbon cycling. Our observations, which capture the effects of mid-summertime thaw and relatively moderate rainfall within the four days prior to sampling (Fig. A1), reflect hydrochemical trends that are likely to vary during the
400   summertime. Constraining these trends across a broader range of hydrologic and permafrost thaw conditions will help to understand variability in mineral weathering effects on inorganic carbon cycling.

3.5 Inorganic Carbon Cycling in Thermokarst-Affected Fluvial Networks

Our study is among the first to evaluate inorganic carbon cycling across gradients of thermokarst disturbance and nested watersheds, enabling an assessment of how catchment chemical characteristics and thermokarst effects
405   integrate across watershed scales. In this framework, our findings support a novel conceptual model of land-freshwater linkages and carbon cycling from headwaters to intermediate scales in thermokarst terrains (Fig. 8). Broadly, these findings reveal fast DIC cycling in headwaters and substantial DIC export downstream. Thermokarst

activity increased CO_2 production in headwaters and fluvial HCO_3^- export across scales by unearthing large amounts of reactive inorganic substrate previously sequestered in permafrost (see also Kokelj et al., 2013; Malone et al.,

410 2013). The striking carbonate weathering and DIC production that we documented in the RTS FM2 runoff indicates that rapid carbon cycling can be expected where thermokarst releases inorganic substrate with limited prior modification (Lacelle et al., 2019). In the larger Stony Creek watershed, DIC cycling was characterized by relatively slower processes associated with HCO_3^- export, which reached magnitudes comparable to watersheds with carbonate denudation by glacial activity (Lafrenière and Sharp, 2005; Striegl et al., 2007). Our findings directly link

415 accelerating thermokarst activity on the Peel Plateau (Segal et al., 2016) with signals of intensifying carbon weathering across the broader Peel and Mackenzie River watersheds (Tank et al., 2016; Zolkos et al., 2018) and suggest that accelerating thermokarst activity will intensify inorganic carbon cycling across broad swaths of the circumpolar north (Zolkos et al., 2018).

Permafrost terrains susceptible to hillslope thermokarst like RTSs are abundant within and outside of former glacial

420 limits across the circumpolar north (Zolkos et al., 2018). Owing to regional variability in geology, glacial activity, climate, and ecosystem history, the mineral composition of permafrost in these regions is likely heterogeneous (Lacelle et al., 2019; Zolkos et al., 2018). The degree to which carbonate weathering is coupled with sulfide oxidation in thermokarst terrains will determine if mineral weathering is a CO_2 sink or source, and thus the strength of abiotic components of the permafrost carbon-climate feedback (Schuur et al., 2015; Zolkos et al., 2018). Current

425 models suggest that mineral weathering across the Peel River watershed is a modest source of CO_2 to the atmosphere, owing to widespread sulfide oxidation coupled with carbonate weathering (Beaulieu et al., 2011). Yet these models do not account for enhanced weathering associated with RTS activity (Tank et al., 2016) and are based on relatively coarse lithologic data which under-represent the abundance of carbonate in exposed bedrock in the southern Richardson and Mackenzie Mountains (Norris, 1985). In the Eurasian north, increasing alkalinity fluxes in

430 recent decades are thought to reflect enhanced H_2CO_3 carbonate weathering coincident with a suite of environmental changes including intensifying permafrost thaw, precipitation, and vegetation activity (Drake et al., 2018b). Integrating thermokarst activity and the mineral composition of permafrost into the next generation of dynamic-numerical biogeochemical models (Beaulieu et al., 2011) will facilitate a better understanding of the effects of permafrost thaw on carbon cycling across rapidly changing northern environments.

435 **4 Conclusions**

Few studies have traced the effects of thermokarst on carbon cycling across watershed scales or within a relatively inorganic-rich permafrost terrain. Here, we find that the climate-driven renewal of deglaciation-phase geomorphic and associated mineral weathering dynamics in the western Canadian Arctic is amplifying CO_2 release in headwaters and exporting substantial HCO_3^- primarily from H_2SO_4 carbonate weathering across watershed scales,

440 despite RTS disturbance across only a fractional proportion of the landscape. Mineral weathering in our study region is both a contemporary and long-term positive feedback to climate change, albeit minor at the scale of inquiry

(Zolkos et al., 2019). Constraining DIC sources and fluvial export across diverse permafrost terrains is critical for understanding a rapidly changing arctic carbon cycle, as our results demonstrate that accelerating thermokarst activity may cause abiotic-inorganic processes to dominate aquatic carbon cycling across broad swaths of the

445 circumpolar north.

Data availability. All data used in this study are available in the supplement.

Supplement. The supplement for this article is available online.

Author contributions. SZ and SET designed the study with contribution from RGS and SVK. SZ led the field
450 research, laboratory analyses, and manuscript writing. JK contributed to geospatial analyses. CEA contributed to laboratory analyses. All authors contributed to manuscript writing.

Competing interests. The authors declare no conflicts of interest.

Acknowledgements. Research was supported by the Natural Sciences and Engineering Research Council of Canada, Campus Alberta Innovates Program, Natural Resources Canada Polar Continental Shelf Program, Environment
455 Canada Science Youth Horizons, UAlberta Northern Research Award, and Arctic Institute of North America Grant-in-Aid. We thank Rosemin Nathoo, Christine Firth, Dempster Collin, Abraham Snowshoe, Sarah Shakil, and Erin Macdonald for assistance in the field. NWT Geological Survey contribution #. Any use of trade, product or firm names in this publication is for descriptive purposes only and does not imply endorsement by the U.S. Government.

References

460 Anderson, S. P.: Biogeochemistry of Glacial Landscape Systems, Annual Review of Earth and Planetary Sciences, 35(1), 375–399, doi:10.1146/annurev.earth.35.031306.140033, 2007.

Beaulieu, E., Goddéris, Y., Labat, D., Roelandt, C., Calmels, D. and Gaillardet, J.: Modeling of water-rock interaction in the Mackenzie basin: Competition between sulfuric and carbonic acids, Chemical Geology, 289(1–2), 114–123, doi:10.1016/j.chemgeo.2011.07.020, 2011.

465 Berner, R. A.: A new look at the long-term carbon cycle, GSA Today, 9(11), 1–6, 1999.

Biskaborn, B. K., Smith, S. L., Noetzli, J., Matthes, H., Vieira, G., Streletskiy, D. A., Schoeneich, P., Romanovsky, V. E., Lewkowicz, A. G., Abramov, A., Allard, M., Boike, J., Cable, W. L., Christiansen, H. H., Delaloye, R., Diekmann, B., Drozdov, D., Etzelmüller, B., Grosse, G., Guglielmin, M., Ingeman-Nielsen, T., Isaksen, K., Ishikawa, M., Johansson, M., Johannsson, H., Joo, A., Kaverin, D., Kholodov, A., Konstantinov, P., Kröger, T.,
470 Lambiel, C., Lanckman, J.-P., Luo, D., Malkova, G., Meiklejohn, I., Moskalenko, N., Oliva, M., Phillips, M., Ramos, M., Sannel, A. B. K., Sergeev, D., Seybold, C., Skryabin, P., Vasiliev, A., Wu, Q., Yoshikawa, K., Zheleznyak, M. and Lantuit, H.: Permafrost is warming at a global scale, Nature Communications, 10(1), doi:10.1038/s41467-018-08240-4, 2019.

475   Bjorkman, A. D., Myers-Smith, I. H., Elmendorf, S. C., Normand, S., Rüger, N., Beck, P. S. A., Blach-Overgaard, A., Blok, D., Cornelissen, J. H. C., Forbes, B. C., Georges, D., Goetz, S. J., Guay, K. C., Henry, G. H. R., HilleRisLambers, J., Hollister, R. D., Karger, D. N., Kattge, J., Manning, P., Prevéy, J. S., Rixen, C., Schaepman-Strub, G., Thomas, H. J. D., Vellend, M., Wilmking, M., Wipf, S., Carbognani, M., Hermanutz, L., Lévesque, E., Molau, U., Petraglia, A., Soudzilovskaia, N. A., Spasojevic, M. J., Tomaselli, M., Vowles, T., Alatalo, J. M., Alexander, H. D., Anadon-Rosell, A., Angers-Blondin, S., Beest, M. te, Berner, L., Björk, R. G., Buchwal, A.,
480   Buras, A., Christie, K., Cooper, E. J., Dullinger, S., Elberling, B., Eskelinen, A., Frei, E. R., Grau, O., Grogan, P., Hallinger, M., Harper, K. A., Heijmans, M. M. P. D., Hudson, J., Hülber, K., Iturrate-Garcia, M., Iversen, C. M., Jaroszynska, F., Johnstone, J. F., Jørgensen, R. H., Kaarlejärvi, E., Klady, R., Kuleza, S., Kulonen, A., Lamarque, L. J., Lantz, T., Little, C. J., Speed, J. D. M., Michelsen, A., Milbau, A., Nabe-Nielsen, J., Nielsen, S. S., Ninot, J. M., Oberbauer, S. F., Olofsson, J., Onipchenko, V. G., Rumpf, S. B., Semenchuk, P., Shetti, R., Collier, L. S., Street, L.
485   E., Suding, K. N., Tape, K. D., Trant, A., Treier, U. A., Tremblay, J.-P., Tremblay, M., Venn, S., Weijers, S., Zamin, T., Boulanger-Lapointe, N., Gould, W. A., Hik, D. S., Hofgaard, A., Jónsdóttir, I. S., Jorgenson, J., Klein, J., et al.: Plant functional trait change across a warming tundra biome, Nature, doi:10.1038/s41586-018-0563-7, 2018.

Bronaugh and Werner: zyp: Zhang + Yue-Pilon trends package, Pacific Climate Impacts Consortium. [online] Available from: https://CRAN.R-project.org/package=zyp, 2013.

490   Calmels, D., Gaillardet, J., Brenot, A. and France-Lanord, C.: Sustained sulfide oxidation by physical erosion processes in the Mackenzie River basin: Climatic perspectives, Geology, 35(11), 1003–1006, doi:10.1130/G24132A.1, 2007.

Campeau, A., Bishop, K., Nilsson, M. B., Klemedtsson, L., Laudon, H., Leith, F. I., Öquist, M. and Wallin, M. B.: Stable Carbon Isotopes Reveal Soil-Stream DIC Linkages in Contrasting Headwater Catchments, Journal of
495   Geophysical Research: Biogeosciences, 123(1), 149–167, doi:10.1002/2017JG004083, 2018.

Clark, I. D. and Fritz, P.: Environmental isotopes in hydrogeology, CRC Press/Lewis Publishers, Boca Raton, FL., 1997.

Cray, H. A. and Pollard, W. H.: Vegetation Recovery Patterns Following Permafrost Disturbance in a Low Arctic Setting: Case Study of Herschel Island, Yukon, Canada, Arctic, Antarctic, and Alpine Research, 47(1), 99–113,
500   doi:10.1657/AAAR0013-076, 2015.

Descolas-Gros, C. and Fontungne, M.: Stable carbon isotope fractionation by marine phytoplankton during photosynthesis, Plant, Cell and Environment, 13(3), 207–218, doi:10.1111/j.1365-3040.1990.tb01305.x, 1990.

Didan, K.: MOD13Q1 MODIS/Terra Vegetation Indices 16-Day L3 Global 250m SIN Grid V006 [Data set]., NASA EOSDIS LP DAAC, doi:doi: 10.5067/MODIS/MOD13Q1.006, 2015.

505   Doctor, D. H., Kendall, C., Sebestyen, S. D., Shanley, J. B., Ohte, N. and Boyer, E. W.: Carbon isotope fractionation of dissolved inorganic carbon (DIC) due to outgassing of carbon dioxide from a headwater stream, Hydrological Processes, 22(14), 2410–2423, doi:10.1002/hyp.6833, 2008.

Drake, T. W., Tank, S. E., Zhulidov, A. V., Holmes, R. M., Gurtovaya, T. and Spencer, R. G. M.: Increasing Alkalinity Export from Large Russian Arctic Rivers, Environmental Science & Technology, 52(15), 8302–8308,
510   doi:10.1021/acs.est.8b01051, 2018a.

Drake, T. W., Guillemette, F., Hemingway, J. D., Chanton, J. P., Podgorski, D. C., Zimov, N. S. and Spencer, R. G. M.: The Ephemeral Signature of Permafrost Carbon in an Arctic Fluvial Network, Journal of Geophysical Research: Biogeosciences, doi:10.1029/2017JG004311, 2018b.

Evans, J. S., Oakleaf, J., Cushman, S. A. and Theobald, D.: An ArcGIS Toolbox for Surface Gradient and
515   Geomorphometric Modeling, version 2.0-0. [online] Available from: http://evansmurphy.wix.com/evansspatial (Accessed 2 December 2015), 2014.

Gentsch, N., Mikutta, R., Shibistova, O., Wild, B., Schnecker, J., Richter, A., Urich, T., Gittel, A., Šantrůčková, H., Bárta, J., Lashchinskiy, N., Mueller, C. W., Fuß, R. and Guggenberger, G.: Properties and bioavailability of particulate and mineral-associated organic matter in Arctic permafrost soils, Lower Kolyma Region, Russia, 520 European Journal of Soil Science, 66(4), 722–734, doi:10.1111/ejss.12269, 2015.

Gordon, N. D., Ed.: Stream hydrology: an introduction for ecologists, 2nd ed., Wiley, Chichester, West Sussex, England ; Hoboken, N.J., 2004.

Hamilton, S. K. and Ostrom, N. E.: Measurement of the stable isotope ratio of dissolved N_2 in ^{15}N tracer experiments, Limnology and Oceanography: Methods, 5(7), 233–240, 2007.

525 Hesslein, R. H., Rudd, J. W. M., Kelly, C., Ramlal, P. and Hallard, K. A.: Carbon dioxide pressure in surface waters of Canadian lakes, in Air-Water Mass Transfer: Selected Papers from the Second International Symposium on Gas Transfer at Water Surfaces, edited by S. C. Wilhelms and J. S. Gulliver, pp. 413–431, American Society of Civil Engineers, New York, New York., 1991.

Hitchon, B. and Krouse, H. R.: Hydrogeochemistry of the surface waters of the Mackenzie River drainage basin, 530 Canada-III. Stable isotopes of oxygen, carbon and sulphur, Geochimica et Cosmochimica Acta, 36, 1337–1357, 1972.

Horgby, Å., Boix Canadell, M., Ulseth, A. J., Vennemann, T. W. and Battin, T. J.: High-Resolution Spatial Sampling Identifies Groundwater as Driver of CO_2 Dynamics in an Alpine Stream Network, J. Geophys. Res. Biogeosci., 124(7), 1961–1976, doi:10.1029/2019JG005047, 2019.

535 Hornby, D. D.: RivEX (Version 10.25). [online] Available from: http://www.rivex.co.uk, 2017.

Huete, A., Didan, K., Miura, T., Rodriguez, E. P., Gao, X. and Ferreira, L. G.: Overview of the radiometric and biophysical performance of the MODIS vegetation indices, Remote Sensing of Environment, 83(1–2), 195–213, doi:10.1016/S0034-4257(02)00096-2, 2002.

Kendall, C., Doctor, D. H. and Young, M. B.: Environmental Isotope Applications in Hydrologic Studies, in 540 Treatise on Geochemistry, vol. 7, edited by H. D. Holland and K. K. Turekian, pp. 273–327, Elsevier, Oxford., 2014.

Kokelj, S. V., Lacelle, D., Lantz, T. C., Tunnicliffe, J., Malone, L., Clark, I. D. and Chin, K. S.: Thawing of massive ground ice in mega slumps drives increases in stream sediment and solute flux across a range of watershed scales, Journal of Geophysical Research: Earth Surface, 118(2), 681–692, doi:10.1002/jgrf.20063, 2013.

545 Kokelj, S. V., Tunnicliffe, J., Lacelle, D., Lantz, T. C., Chin, K. S. and Fraser, R.: Increased precipitation drives mega slump development and destabilization of ice-rich permafrost terrain, northwestern Canada, Global and Planetary Change, 129, 56–68, doi:10.1016/j.gloplacha.2015.02.008, 2015.

Kokelj, S. V., Lantz, T. C., Tunnicliffe, J., Segal, R. and Lacelle, R.: Climate-driven thaw of permafrost preserved glacial landscapes, northwestern Canada, Geology, 45(4), 371–374, doi:10.1130/G38626.1, 2017a.

550 Kokelj, S. V., Tunnicliffe, J. F. and Lacelle, D.: The Peel Plateau of Northwestern Canada: An Ice-Rich Hummocky Moraine Landscape in Transition, in Landscapes and Landforms of Western Canada, edited by O. Slaymaker, pp. 109–122, Springer International Publishing, Cham., 2017b.

Kuznetsova, A., Brockhoff, P. B. and Christensen, R. H. B.: Package 'lmerTest.', 2018.

Lacelle, D., Fontaine, M., Pellerin, A., Kokelj, S. V. and Clark, I. D.: Legacy of Holocene Landscape Changes on 555 Soil Biogeochemistry: A Perspective From Paleo-Active Layers in Northwestern Canada, J. Geophys. Res. Biogeosci., 2018JG004916, doi:10.1029/2018JG004916, 2019.

Lafrenière, M. J. and Sharp, M. J.: A comparison of solute fluxes and sources from glacial and non-glacial catchments over contrasting melt seasons, Hydrological Processes, 19(15), 2991–3012, doi:10.1002/hyp.5812, 2005.

560 Lehn, G. O., Jacobson, A. D., Douglas, T. A., McClelland, J. W., Barker, A. J. and Khosh, M. S.: Constraining seasonal active layer dynamics and chemical weathering reactions occurring in North Slope Alaskan watersheds with major ion and isotope ($\delta^{34}S_{SO4}$, $\delta^{13}C_{DIC}$, $^{87}Sr/^{86}Sr$, $\delta^{44/40}Ca$, and $\delta^{44/42}Ca$) measurements, Geochimica et Cosmochimica Acta, 217, 399–420, doi:10.1016/j.gca.2017.07.042, 2017.

Littlefair, C. A., Tank, S. E. and Kokelj, S. V.: Retrogressive thaw slumps temper dissolved organic carbon delivery to streams of the Peel Plateau, NWT, Canada, Biogeosciences, 14(23), 5487–5505, doi:10.5194/bg-14-5487-2017, 565 2017.

Lurry, D. L. and Kolbe, C. M.: Interagency Field Manual for the Collection of Water-Quality Data, USGS., 2000.

Malone, L., Lacelle, D., Kokelj, S. and Clark, I. D.: Impacts of hillslope thaw slumps on the geochemistry of permafrost catchments (Stony Creek watershed, NWT, Canada), Chemical Geology, 356, 38–49, doi:10.1016/j.chemgeo.2013.07.010, 2013.

570 Millero, F. J.: The thermodynamics of the carbonate system in seawater, Geochimica et Cosmochimica Acta, 43, 1651–1661, 1979.

Mook, W. G., Bommerson, J. C. and Staverman, W. H.: Carbon isotope fractionation between dissolved bicarbonate and gaseous carbon dioxide, Earth and Planetary Science Letters, 22(2), 169–176, 1974.

Norris, D. K.: Geology of the Northern Yukon and Northwestern District of Mackenzie, 1985.

575 Parkhurst, D. I. and Appelo, C. A. J.: Description of input and examples for PHREEQC version 3 – A computer program for speciation, batch- reaction, one-dimensional transport, and inverse geochemical calculations, vol. A43, p. 497, U.S. Geological Survey. [online] Available from: http://pubs.usgs.gov/tm/06/a43, 2013.

Pierrot, D., Lewis, E. and Wallace, D. W. R.: MS Excel program developed for CO_2 system calculations. [online] Available from: doi:10.3334/CDIAC/otg. CO2SYS_XLS_CDIAC105a, 2006.

580 Poulin, B. A., Ryan, J. N. and Aiken, G. R.: Effects of Iron on Optical Properties of Dissolved Organic Matter, Environmental Science & Technology, 48(17), 10098–10106, doi:10.1021/es502670r, 2014.

R Core Team: R: A Language and Environment for Statistical Computing, R Foundation for Statistical Computing, Vienna, Austria. [online] Available from: http://www.r-project.org/, 2018.

Rawlins, M. A., Steele, M., Holland, M. M., Adam, J. C., Cherry, J. E., Francis, J. A., Groisman, P. Y., Hinzman, L. 585 D., Huntington, T. G., Kane, D. L., Kimball, J. S., Kwok, R., Lammers, R. B., Lee, C. M., Lettenmaier, D. P., McDonald, K. C., Podest, E., Pundsack, J. W., Rudels, B., Serreze, M. C., Shiklomanov, A., Skagseth, Ø., Troy, T. J., Vörösmarty, C. J., Wensnahan, M., Wood, E. F., Woodgate, R., Yang, D., Zhang, K. and Zhang, T.: Analysis of the Arctic System for Freshwater Cycle Intensification: Observations and Expectations, Journal of Climate, 23(21), 5715–5737, doi:10.1175/2010JCLI3421.1, 2010.

590 Riley, S. J., DeGloria, S. D. and Elliot, R.: A terrain ruggedness index that quantifies topographic heterogeneity, Intermountain Journal of Sciences, 5(1–4), 23–27, 1999.

Sander, R.: Compilation of Henry's law constants (version 4.0) for water as solvent, Atmos. Chem. Phys., 15(8), 4399–4981, doi:10.5194/acp-15-4399-2015, 2015.

Schuur, E. A. G., McGuire, A. D., Schädel, C., Grosse, G., Harden, J. W., Hayes, D. J., Hugelius, G., Koven, C. D., 595 Kuhry, P., Lawrence, D. M., Natali, S. M., Olefeldt, D., Romanovsky, V. E., Schaefer, K., Turetsky, M. R., Treat, C.

C. and Vonk, J. E.: Climate change and the permafrost carbon feedback, Nature, 520(7546), 171–179, doi:10.1038/nature14338, 2015.

Segal, R. A., Lantz, T. C. and Kokelj, S. V.: Acceleration of thaw slump activity in glaciated landscapes of the Western Canadian Arctic, Environmental Research Letters, 11(3), 034025, doi:10.1088/1748-9326/11/3/034025, 2016.

Serreze, M. C. and Barry, R. G.: Processes and impacts of Arctic amplification: A research synthesis, Global and Planetary Change, 77(1–2), 85–96, doi:10.1016/j.gloplacha.2011.03.004, 2011.

Sharp, M., Tranter, M., Brown, G. H. and Skidmore, M.: Rates of chemical denudation and CO_2 drawdown in a glacier-covered alpine catchment, Geology, 23(1), 61–64, 1995.

St. Pierre, K. A., St. Louis, V. L., Schiff, S. L., Lehnherr, I., Dainard, P. G., Gardner, A. S., Aukes, P. J. K. and Sharp, M. J.: Proglacial freshwaters are significant and previously unrecognized sinks of atmospheric CO_2, Proc Natl Acad Sci USA, 201904241, doi:10.1073/pnas.1904241116, 2019.

Stallard, R. F. and Edmond, J. M.: Geochemistry of the Amazon: 2. The Influence of Geology and Weathering Environment on the Dissolved Load, Journal of Geophysical Research, 88(C14), 9671–9688, 1983.

Striegl, R. G., Dornblaser, M. M., Aiken, G. R., Wickland, K. P. and Raymond, P. A.: Carbon export and cycling by the Yukon, Tanana, and Porcupine rivers, Alaska, 2001-2005, Water Resources Research, 43(2), doi:10.1029/2006WR005201, 2007.

Stubbins, A., Silva, L. M., Dittmar, T. and Van Stan, J. T.: Molecular and Optical Properties of Tree-Derived Dissolved Organic Matter in Throughfall and Stemflow from Live Oaks and Eastern Red Cedar, Frontiers in Earth Science, 5, doi:10.3389/feart.2017.00022, 2017.

Stumm, W. and Morgan, J. J.: Aquatic Chemistry: Chemical Equilibria and Rates in Natural Waters, 3rd ed., John Wiley & Son, Inc., New York., 1996.

Tank, S. E., Striegl, R. G., McClelland, J. W. and Kokelj, S. V.: Multi-decadal increases in dissolved organic carbon and alkalinity flux from the Mackenzie drainage basin to the Arctic Ocean, Environmental Research Letters, 11(5), 054015, doi:10.1088/1748-9326/11/5/054015, 2016.

Toohey, R. C., Herman-Mercer, N. M., Schuster, P. F., Mutter, E. A. and Koch, J. C.: Multidecadal increases in the Yukon River Basin of chemical fluxes as indicators of changing flowpaths, groundwater, and permafrost, Geophysical Research Letters, 43(23), 12,120-12,130, doi:10.1002/2016GL070817, 2016.

Torres, M. A., Moosdorf, N., Hartmann, J., Adkins, J. F. and West, A. J.: Glacial weathering, sulfide oxidation, and global carbon cycle feedbacks, Proceedings of the National Academy of Sciences, 114(33), 8716–8721, doi:10.1073/pnas.1702953114, 2017.

Turner, J. V.: Kinetic fractionation of carbon-13 during calcium carbonate precipitation, Geochimica et Cosmochimica Acta, 46, 1183–1191, doi:10.1016/0016-7037(82)90004-7, 1982.

Vonk, J. E., Tank, S. E., Mann, P. J., Spencer, R. G. M., Treat, C. C., Striegl, R. G., Abbott, B. W. and Wickland, K. P.: Biodegradability of dissolved organic carbon in permafrost soils and aquatic systems: a meta-analysis, Biogeosciences, 12(23), 6915–6930, doi:10.5194/bg-12-6915-2015, 2015.

Vonk, J. E., Tank, S. E. and Walvoord, M. A.: Integrating hydrology and biogeochemistry across frozen landscapes, Nat Commun, 10(1), 5377, doi:10.1038/s41467-019-13361-5, 2019.

635   Wadham, J. L., Hawkings, J. R., Tarasov, L., Gregoire, L. J., Spencer, R. G. M., Gutjahr, M., Ridgwell, A. and Kohfeld, K. E.: Ice sheets matter for the global carbon cycle, Nat Commun, 10(1), 3567, doi:10.1038/s41467-019-11394-4, 2019.

Walvoord, M. A. and Kurylyk, B. L.: Hydrologic Impacts of Thawing Permafrost—A Review, Vadose Zone Journal, 15(6), 0, doi:10.2136/vzj2016.01.0010, 2016.

640   Weishaar, J. L., Aiken, G. R., Bergamaschi, B. A., Fram, M. S., Fujii, R. and Mopper, K.: Evaluation of Specific Ultraviolet Absorbance as an Indicator of the Chemical Composition and Reactivity of Dissolved Organic Carbon, Environmental Science & Technology, 37(20), 4702–4708, doi:10.1021/es030360x, 2003.

Weiss, R. F.: Carbon dioxide in water and seawater: the solubility of a non-ideal gas, Marine Chemistry, 2(3), 203–215, 1974.

645   Wiesenburg, D. A. and Guinasso, N. L.: Equilibrium solubilities of methane, carbon monoxide, and hydrogen in water and sea water, Journal of Chemical and Engineering Data, 24(4), 356–360, 1979.

Yue, S., Pilon, P., Phinney, B. and Cavadias, G.: The influence of autocorrelation on the ability to detect trend in hydrological series, Hydrological Processes, 16(9), 1807–1829, doi:10.1002/hyp.1095, 2002.

Zhang, J., Quay, P. D. and Wilbur, D. O.: Carbon isotope fractionation during gas-water exchange and dissolution of CO_2, Geochimica et Cosmochimica Acta, 59(1), 107–114, 1995.

650   Zolkos, S., Tank, S. E. and Kokelj, S. V.: Mineral Weathering and the Permafrost Carbon-Climate Feedback, Geophysical Research Letters, doi:10.1029/2018GL078748, 2018.

Zolkos, S., Tank, S. E., Striegl, R. G. and Kokelj, S. V.: Thermokarst Effects on Carbon Dioxide and Methane Fluxes in Streams on the Peel Plateau (NWT, Canada), J. Geophys. Res. Biogeosci., 2019JG005038, doi:10.1029/2019JG005038, 2019.

655   Zuur, A. F., Ed.: Mixed effects models and extensions in ecology with R, Springer, New York, NY., 2009.

Zuur, A. F., Ieno, E. N. and Elphick, C. S.: A protocol for data exploration to avoid common statistical problems, Methods in Ecology and Evolution, 1(1), 3–14, doi:10.1111/j.2041-210X.2009.00001.x, 2010.

659 **Table 1.** Geochemical characteristics of tributary and mainstem sites along Dempster and Stony Creeks. [†]Sampled
660 on July 30, 2017, while other retrogressive thaw slump (RTS) FM2 runoff samples were collected on July 31, 2017.
661 RTS FM2 runoff site #5 was nearest the confluence with Dempster Creek (Fig. 1). Area = watershed area.

Type	Site	pH	pCO_2 (µatm)	CO_2 (µM)	HCO_3^- (µM)	CO_3^{2-} (µM)	DIC (uM)	Cond (µS cm⁻¹)	$\delta^{13}C_{DIC}$ (‰VPDB)	$\delta^{13}C_{CO2}$ (‰VPDB)	DOC (µM)	$SUVA_{254}$ (L mgC⁻¹ m⁻¹)	TSS (mg L⁻¹)	Area (km²)	RTS (% area)
RTS FM2 (Runoff)	1	7.72	1046	43	1510	5.2	1559	1370	–	-12.1	758	1.85	–	–	–
	2	7.51	1534	60	1439	3.5	1502	1816	–	-11.4	–	–	–	–	–
	3	7.71	914	37	1419	5.4	1462	1920	–	-10.3	–	–	–	–	–
	4	7.73	878	38	1391	5.1	1433	1903	–	-10.0	–	–	–	–	–
	5	7.80	742	33	1386	5.8	1424	1986	–	-11.2	–	–	–	–	–
	5[†]	7.82	691	29	1450	7.1	1487	1653	-1.0	-11.6	726	1.84	15805	–	–
Dempster (Mainstem)	1	5.82	2467	124	115	0.0	239	52	-15.0	-21.6	960	3.66	5	2	0.00
	2	7.55	686	35	1321	4.8	1361	958	-4.2	-16.0	790	2.53	11795	16	3.18
	3	7.54	656	31	1073	3.6	1107	655	-5.3	-15.6	823	2.93	9165	24	2.18
	4	7.35	600	30	946	2.9	978	416	-5.7	-18.5	1156	3.28	2797	57	1.19
Dempster (Tributary)	2	7.56	836	50	1233	2.8	1286	390	-10.5	-21.3	1053	3.46	26	2	0.00
	3	7.32	478	23	561	1.3	586	171	-7.2	-18.1	1241	3.65	985	11	1.47
	4	7.30	552	27	697	1.7	726	236	-8.0	-16.5	922	3.61	223	168	0.40
Stony (Mainstem)	1	5.66	543	33	33	0.0	65	406	-11.6	-13.8	102	1.29	3	83	0.00
	2	6.37	448	25	69	0.0	94	396	-8.0	-15.1	124	1.58	920	136	0.01
	3	7.01	473	27	112	0.0	139	334	-6.9	-15.3	202	2.16	799	176	0.27
	4	6.69	444	25	248	0.2	273	283	-8.9	-17.6	306	2.77	462	479	0.39
	5	7.20	482	27	325	0.4	353	279	-8.4	-17.6	364	3.09	507	490	0.38
	6	7.33	461	25	382	0.5	408	290	-7.8	-18.1	385	3.01	665	626	0.33
	7	7.30	461	25	409	0.6	435	293	-8.1	-18.1	390	2.99	761	689	0.32
	8	7.30	519	27	461	0.7	489	279	-7.8	-18.1	551	3.19	1073	995	0.36
Stony (Tributary)	1	5.00	451	25	1	0.0	26	524	-15.6	-12.3	101	0.73	5	26	0.00
	2	6.71	501	28	449	0.7	478	226	-5.0	-15.9	437	2.22	39568	7	3.50
	3	7.11	448	26	338	0.4	365	148	-9.3	-18.0	458	3.12	10	59	0.16
	4	6.53	572	32	375	0.4	407	245	-8.5	-19.4	550	3.31	704	194	0.67
	5	7.00	494	26	601	1.3	628	479	-7.0	-18.0	596	2.88	1270	104	0.13
	6	7.37	498	27	633	1.4	661	260	-8.0	-18.3	1142	3.34	1936	38	0.20
	7	7.32	475	26	570	1.2	597	230	-10.7	-18.0	1078	3.56	1258	227	0.60

662

Table 2. Characteristics of Stony Creek tributary watersheds. RTS = retrogressive thaw slump. The Stony Creek watershed contained 109 RTSs, 92 of which were in the major tributaries of the Stony Creek mainstem. TR = terrain roughness. EVI = enhanced vegetation index. Values were used in the multiple linear regression model to determine the drivers of HCO_3^- yields in Stony Creek tributary watersheds. Model results are shown in the lower panel. Covariates eliminated during model selection (RTS_n, EVI) are not reflected in the lower panel or final model: HCO_3^- yield = $2818ln$Water yield + $183RTS_{area}$ − $101TR$ + 2818.

Tributary	HCO_3^- yield ($\mu M\ m^{-2}\ d^{-1}$)	Water yield (cm d^{-1})	RTS (% area)	RTS (n)	Mean TR (m)	Mean EVI
1	1.6	0.20	0.00	0	16.2	0.28
2	2721	0.61	3.50	6	3.4	0.48
3	616	0.18	0.16	3	6.7	0.45
4	155	0.04	0.67	50	4.5	0.45
5	742	0.12	0.31	11	4.7	0.46
6	1791	0.28	0.20	8	2.7	0.47
7	397	0.07	0.60	14	3.6	0.45

Covariate	Estimate	t	p
lnWater yield	774	6.6	0.01
RTS_{area}	183	2.0	0.14
TR	-101	-5.0	0.02
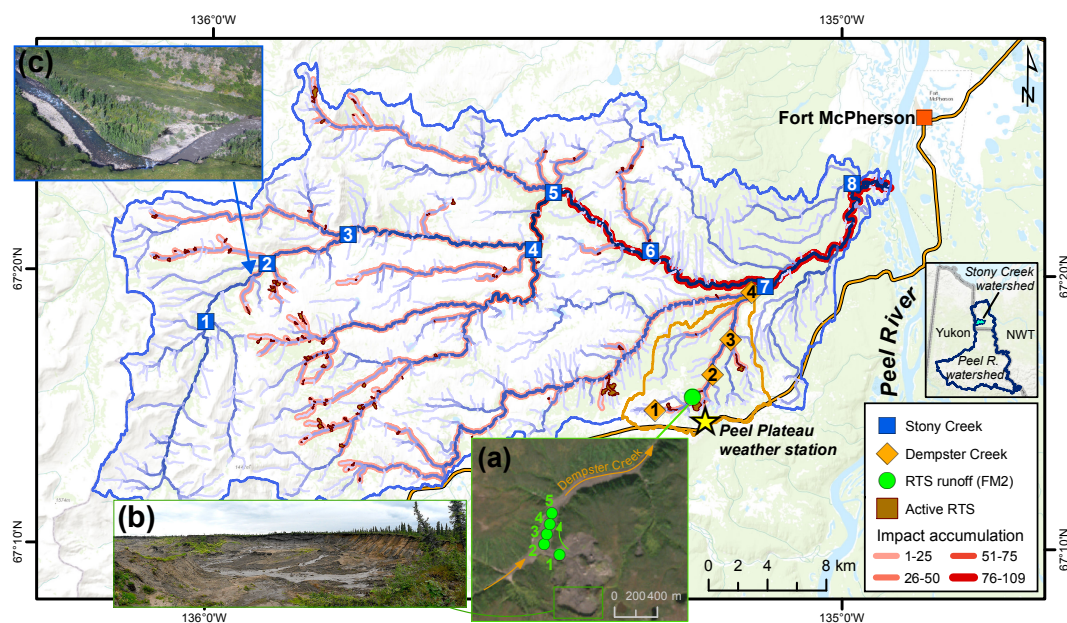
Figure 1. Sampling sites on the Peel Plateau (NWT, Canada). Water samples were collected along the mainstem Dempster and Stony Creeks ($n = 12$) and major tributaries ($n = 10$), and from the rill runoff at retrogressive thaw slump (RTS) FM2. Site numbers are given within symbols (Table A1). Basemap from Esri ArcGIS Online. (**a**) RTS FM2 runoff transect sampling scheme. Satellite image of RTS FM2 in September 2017 obtained from Copernicus Sentinel data (European Space Agency, https://sentinel.esa.int/). (**b**) A portion of the RTS FM2 headwall (see location in (**a**)). RTS FM2 spans ~40 ha, its headwall reaches ~25 m in height, and the debris tongue contains ~10^6 m³ of sediment (Kokelj et al., 2013). (**c**) Aerial photograph of Stony Creek where it was first impacted by RTS activity. RTS impact accumulation (see Methods Sect. 2.6) represents the number of active RTSs (total $n = 109$) affecting upstream reaches. Basemap: Esri ArcGIS Online © OpenStreetMap contributors, GIS User Community.
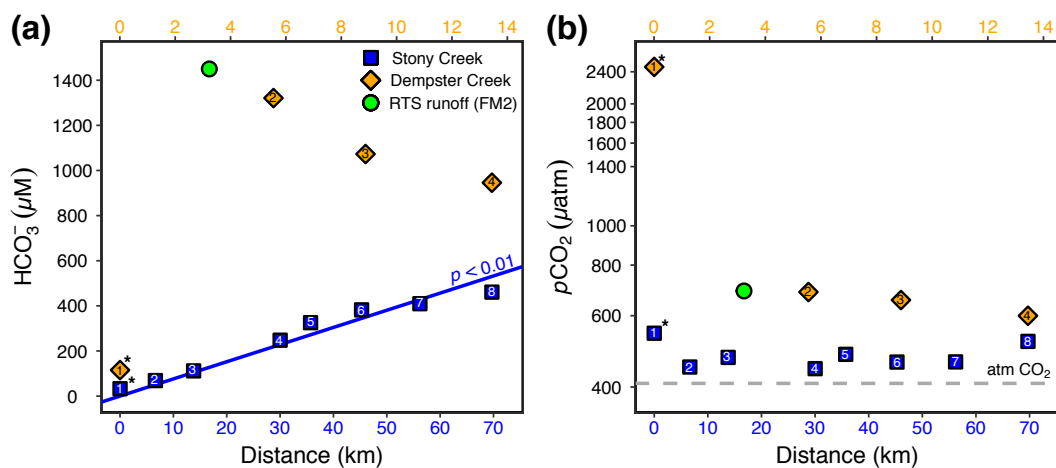
681
682 **Figure 2.** (**a**) HCO_3^- and (**b**) pCO_2 trends along the mainstem Stony and Dempster Creeks (see locations in Fig. 1).
683 The retrogressive thaw slump (RTS) FM2 runoff is a tributary to Dempster Creek. Note different x-axis scales for
684 the two transects. Regression line in (**a**) is from the Mann-Kendall test (see text for details). Dempster Creek enters
685 Stony Creek at Site 7. Site numbers are given within symbols (Table A1). *Site was not affected by RTSs.
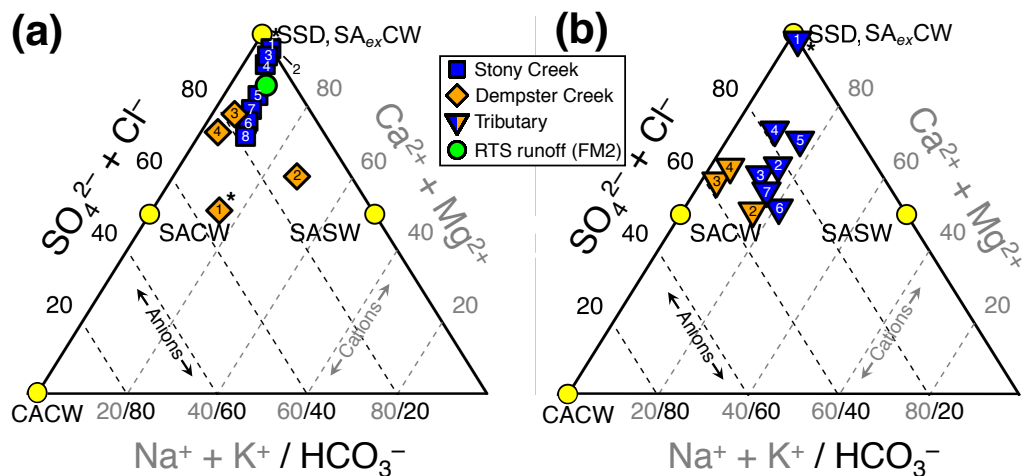
686
687 **Figure 3.** Piper diagrams (modified to show the upper half of the diamond plot) showing stream chemistry of the (**a**)
688 mainstem sites and (**b**) tributary and retrogressive thaw slump (RTS) FM2 runoff sites. Axes and corresponding text
689 in gray and black reflect the proportions of cations and anions, respectively. Mineral weathering end-members were
690 derived from the proportional concentration (meq L^{-1}) of solutes generated by H_2CO_3 carbonate weathering (CACW,
691 Eq. A1), H_2SO_4 carbonate weathering (SACW, Eq. A3), H_2SO_4 silicate weathering (SASW, Eq. A4), sulfate salt
692 (gypsum) dissolution (SSD, Eq. A5), and carbonate weathering by H_2SO_4 in excess (SA$_{ex}$CW, Eq. A7). Site
693 numbers given within symbols (Table A1). ***** Site was not affected by RTSs.
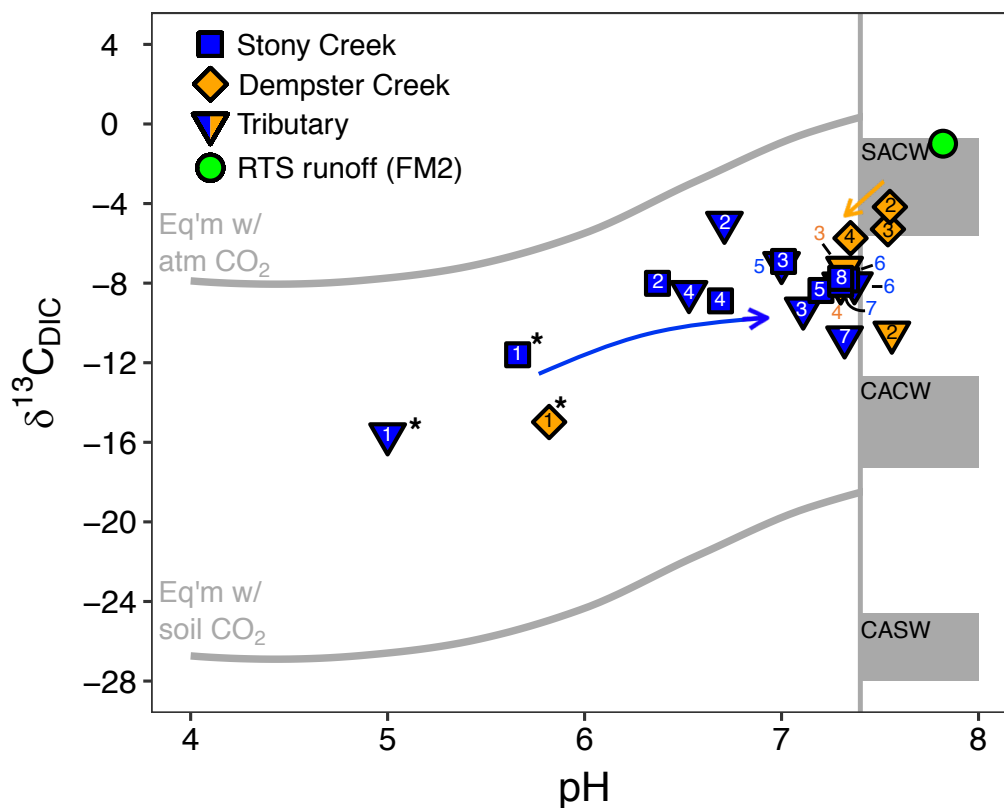
Figure 4. The pH and composition of dissolved inorganic carbon stable isotopes ($\delta^{13}C_{DIC}$) in streams. The upper and lower reference lines depict theoretical end-members for equilibrium reactions (mixing with atmospheric and biotic CO_2, respectively). Gray boxes span theoretical end-member values for kinetically controlled mineral weathering reactions (SACW = H_2SO_4 carbonate weathering, CACW = H_2CO_3 carbonate weathering, CASW = H_2CO_3 silicate weathering). The vertical line corresponds to the pH at which $\geq$ 90% of DIC is HCO_3^-, for the mean observed stream water temperature (11.7˚C). At pH < 7.4, $\delta^{13}C_{DIC}$ values primarily reflect equilibrium (rather than kinetic) controls on DIC cycling. Arrows reflect increasing downstream distance from the headwaters in Stony Creek and from the first retrogressive thaw slump (RTS) affected site in Dempster Creek. Site numbers given within symbols (Table A1). *Site was not affected by RTSs.
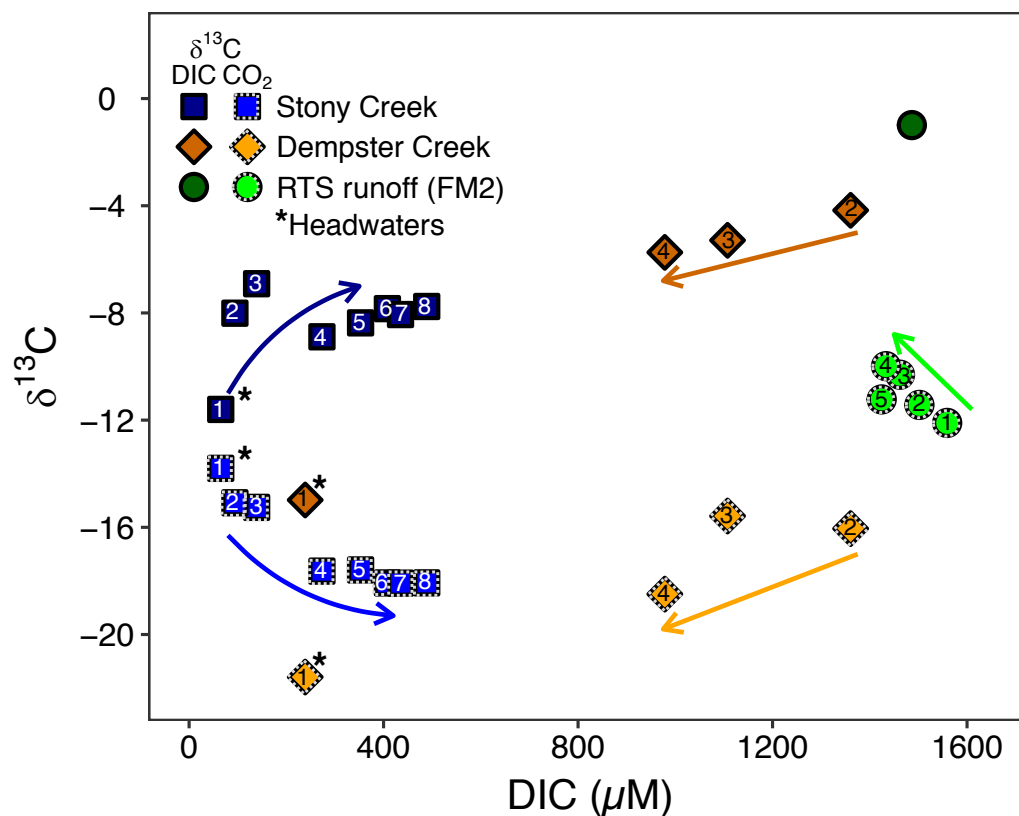
Figure 5. The composition of DIC and CO_2 stable isotopes at varying DIC concentrations along the Dempster and
Stony Creek mainstems, and in the rill runoff of retrogressive thaw slump (RTS) FM2. Arrows reflect increasing
downstream distance from headwaters in Stony Creek, from the first RTS-affected site in Dempster Creek, and from
the start of the FM2 runoff transect. Site numbers given within symbols (Table A1). *Site in headwaters and not
affected by RTSs.
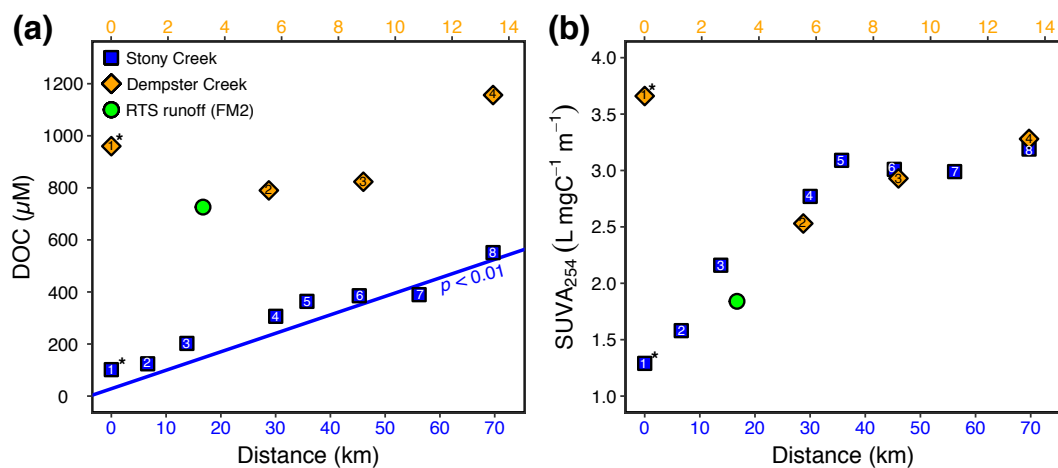
711
712 **Figure 6.** Trends in (**a**) DOC and (**b**) SUVA$_{254}$ along the mainstem Stony and Dempster Creeks (see locations in
713 Fig. 1). Retrogressive thaw slump (RTS) FM2 runoff is a tributary to Dempster Creek. Note different x-axis scales
714 for the two transects. Regression line in (**a**) is from the Mann-Kendall test (see text for details). Dempster Creek
715 enters Stony Creek at 58.5 km downstream. Site numbers given within symbols (Table A1). *****Site was not affected
716 by RTSs.
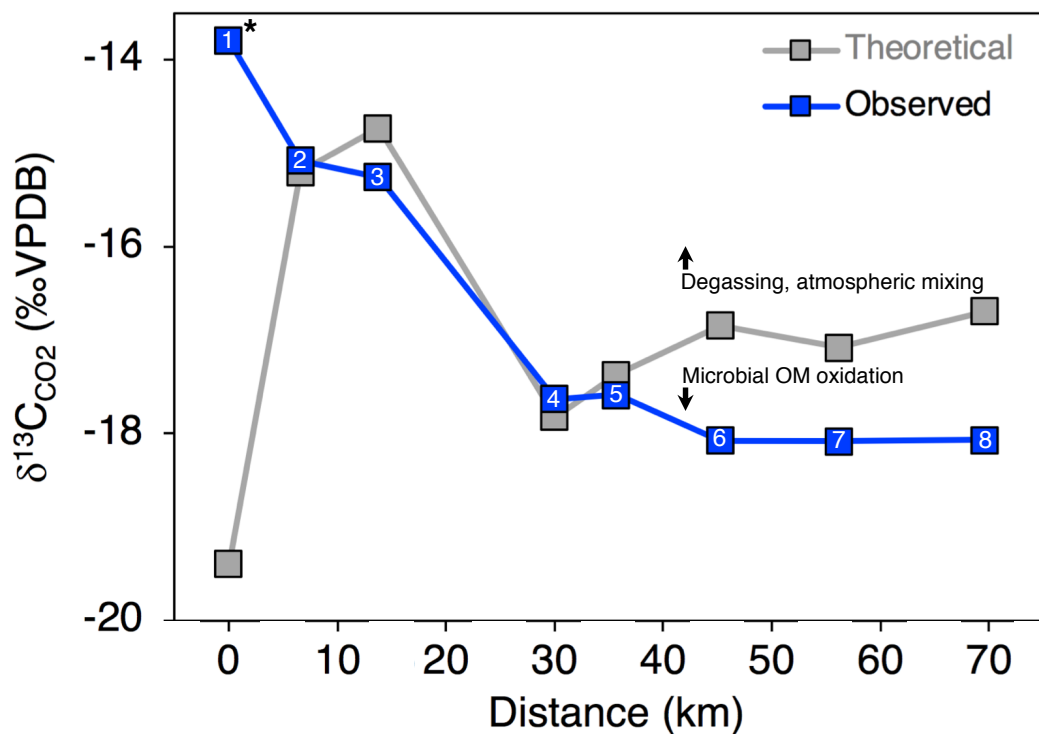
Figure 7. Observed and expected $\delta^{13}C_{CO2}$ values along the Stony Creek mainstem. Theoretical $\delta^{13}C_{CO2}$ values were calculated as detailed in Sect. 2.6 and reflect changes in CO_2 due to DIC speciation (i.e. $H_2CO_3 \rightleftharpoons H^+ + HCO_3^-$, Eq. A8). Deviation from theoretical $\delta^{13}C_{CO2}$ values by observed values thus indicates isotopic effects from degassing and/or microbial oxidation of organic matter (OM), as indicated by the arrows. Site numbers given within symbols (Table A1). *Site was not affected by retrogressive thaw slumps.
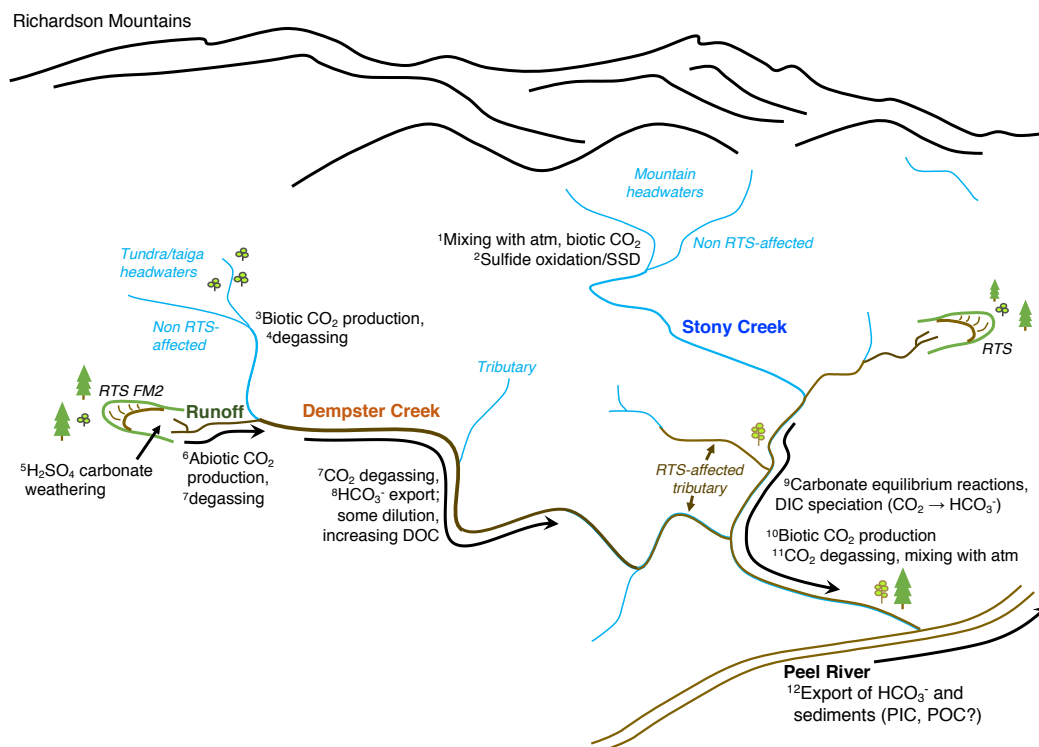
Figure 8. Conceptual model of fluvial inorganic carbon cycling in a glaciated thermokarst terrain (Peel Plateau, NWT). Evidence for processes in the diagram are shown as numbers and discussed in the main text: [1]Low CO_2, intermediate $\delta^{13}C_{CO2}$; [2]High SO_4^{2-} and ^{13}C-enriched $\delta^{13}C_{DIC}$; [3]Low $\delta^{13}C_{CO2}$; [4]decreasing CO_2; [5]High HCO_3^-, pH, and $\delta^{13}C_{DIC}$; [6,7]Relatively ^{13}C-enriched $\delta^{13}C_{DIC}$ and increasing $\delta^{13}C_{CO2}$; [8]high but decreasing HCO_3^- and conductivity; [9]Increasing HCO_3^-, pH, and $\delta^{13}C_{DIC}$, and $\delta^{13}C_{CO2}$ reflective of DIC speciation; [10]$\delta^{13}C_{CO2}$ reflective of microbial organic matter (OM) oxidation; [11]Saturated and stable $p$$CO_2$; [12]Kokelj et al. (2013), Zolkos et al. (2018).

Appendices

Table A1. Sampling site characteristics. Retrogressive thaw slump (RTS) FM2 runoff was a tributary to Dempster Creek (confluence upstream of site 2) and Dempster Creek was a tributary to Stony Creek (confluence upstream of site 8). Coordinates reported in decimal degrees. †FM2 runoff distances are in m. *Site was not affected by RTSs.

Creek	Site	Type	Latitude (DD)	Longitude (DD)	Sampling date	Distance (km)†	Elevation (m)
RTS FM2	1	Runoff	67.25639	-135.23422	7/31/17	0	–
RTS FM2	2	Runoff	67.25726	-135.23756	7/31/17	220	–
RTS FM2	3	Runoff	67.25813	-135.23700	7/31/17	330	–
RTS FM2	4	Runoff	67.25894	-135.23636	7/31/17	440	–
RTS FM2	5	Runoff	67.25986	-135.23595	7/31/17	550	–
RTS FM2	5	Runoff	67.25981	-135.23587	7/30/17	–	271
Dempster	1*	Mainstem	67.25181	-135.29456	7/31/17	0	407
Dempster	2	Mainstem	67.27364	-135.20409	7/29/17	5.6	194
Dempster	3	Mainstem	67.29500	-135.17570	7/27/17	8.9	132
Dempster	4	Mainstem	67.32336	-135.14133	7/27/17	13.5	67
Dempster	2	Tributary	67.27364	-135.20367	7/29/17	–	–
Dempster	3	Tributary	67.29497	-135.17538	7/27/17	–	–
Dempster	4	Tributary	67.32414	-135.14252	7/27/17	–	–
Stony	1*	Mainstem	67.30280	-136.00468	7/27/17	0.0	575
Stony	2	Mainstem	67.33878	-135.90912	7/27/17	6.6	474
Stony	3	Mainstem	67.35704	-135.78165	7/25/17	13.8	382
Stony	4	Mainstem	67.34913	-135.48802	7/25/17	30.0	230
Stony	5	Mainstem	67.38380	-135.45747	7/25/17	35.7	184
Stony	6	Mainstem	67.34879	-135.30302	7/25/17	45.3	123
Stony	7	Mainstem	67.32732	-135.12160	7/25/17	56.2	57
Stony	8	Mainstem	67.39000	-134.98380	7/25/17	69.7	6
Stony	1*	Tributary	67.30367	-136.00421	7/27/17	–	–
Stony	2	Tributary	67.33933	-135.90836	7/27/17	–	–
Stony	3	Tributary	67.35719	-135.78311	7/25/17	–	–
Stony	4	Tributary	67.34860	-135.48773	7/25/17	–	–
Stony	5	Tributary	67.38467	-135.45607	7/25/17	–	–
Stony	6	Tributary	67.34882	-135.30196	7/25/17	–	–
Stony	7	Tributary	67.32703	-135.12213	7/25/17	–	–

734

735   **Table A2.** Mineral weathering equations used to create Piper diagram end-members. H_2CO_3 = carbonic acid, H_2SO_4
736   = sulfuric acid. H_2CO_3 includes dissolved CO_2.

Eq.	Reaction	Acronym	Equation	Reference
A1	Carbonic acid carbonate weathering	CACW	$H_2CO_3 + (Ca,Mg)CO_3 \rightarrow (Ca^{2+},Mg^{2+}) + 2HCO_3^-$	Lehn et al. (2017)
A2	Carbonic acid silicate weathering	CASW	$2H_2CO_3 + 3H_2O + (Ca,Mg)Al_2Si_2O_8 \rightarrow (Ca^{2+},Mg^{2+}) + 2HCO_3^- + 2Al_2Si_2O_5(OH)_4$	Lehn et al. (2017)
A3	Sulfuric acid carbonate weathering	SACW	$H_2SO_4 + 2(Ca,Mg)CO_3 \rightarrow 2(Ca^{2+},Mg^{2+}) + SO_4^{2-} + 2HCO_3^-$	Lehn et al. (2017)
A4	Sulfuric acid silicate weathering	SASW	$H_2SO_4 + H_2O + (Ca,Mg)Al_2Si_2O_8 \rightarrow (Ca^{2+},Mg^{2+}) + SO_4^{2-} + Al_2Si_2O_5(OH)_4$	Lehn et al. (2017)
A5	Sulfate salt dissolution	SSD	$(Ca,Mg)SO_4 \rightarrow (Ca^{2+},Mg^{2+}) + SO_4^{2-}$	Lehn et al. (2017)
A6	Sulfide oxidation	–	$FeS_2 + 15/4O_2 + 7/2H_2O \rightarrow Fe(OH)_3 + 2H^+ + SO_4^{2-}$	Calmels et al. (2007)
A7	Carbonate weathering by H_2SO_4 in excess	$SA_{ex}CW$	$2H_2SO_4 + CaMg(CO_3)_2 \rightarrow Ca^{2+} + Mg^{2+} + 2SO_4^{2-} + 2H_2CO_3$	Stallard and Edmond (1983)
A8	DIC speciation	–	$H_2O + CO_{2(g)} \rightleftharpoons H_2CO_3 \rightleftharpoons H^+ + HCO_3^- \rightleftharpoons 2H^+ + CO_3^{2-}$	Stumm and Morgan (1996)

737
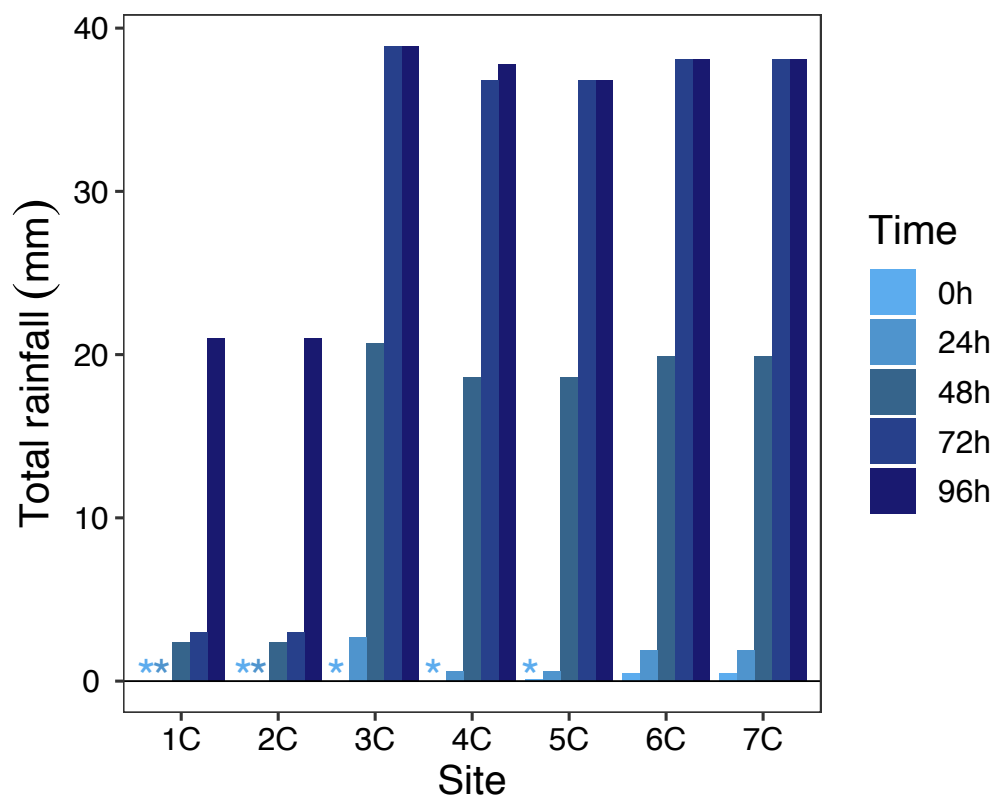
738
739 **Figure A1.** Total rainfall in 24 h increments preceding the sampling of each Stony Creek tributary. Rainfall data
740 were obtained from a Government of Northwest Territories weather station on the Peel Plateau located near the RTS
741 FM2. Locations of tributary sampling sites and the weather station are shown in Fig. 1. *Indicates no rainfall in the
742 24 h window.